Nonmodal Analysis of Temporal Transverse Shear Instabilities in Shallow Flows

Transient Energy Growth in Time

Yarzar Tun

Thesis submitted in partial fulfillment of the requirements for
The degree of Master of Applied Science in Civil Engineering

Thesis Supervisor: Dr. Abdolmajid Mohammadian

uOttawa

Department of Civil Engineering
Faculty of Engineering
University of Ottawa
Ottawa, Ontario, Canada

Abstract

Shallow flows are those whose width is significantly larger than their depth. In these types of flows, two dimensional coherent structures can be generated and can influence the flow greatly by the lateral transfer of mass and momentum. The development of coherent structures as a result of flow instabilities has been a topic of interest for environmental fluid mechanics for decades. Studies on the use of linear modal stability analysis is commonly found in literature. However, the relatively recent development in the field of hydrodynamic stability suggests that the traditional linear modal stability analysis does not describe the behaviour of the perturbations in finite time. The discrepancy between asymptotic behaviour and finite time behaviour is particularly large in shear driven flows and it is most likely to be the case for shallow flows. This study aims to provide a better understanding of finite time growth of perturbation energy in shallow flows. The three cases of shallow flows evaluated are the mixing layer, jet and wake. The critical cases are obtained through the linear modal analysis and nonmodal analysis was conducted to show the transient behaviour in finite time for what is so-called marginally stable. Finally, the thesis concludes by generalizing the finite time energy growth in the S-k space.

Declaration

This thesis describes research carried out in the Department of Civil Engineering, Faculty of Engineering, University of Ottawa. The dissertation is the result of my own work and includes nothing which is the outcome of work done in collaboration, except where specifically indicated in the text. The numerical calculations presented were computed using my own MATLAB code, with the exception of pseudospectral portraits, which were done using the Eigtools MATLAB package as cited in the thesis. No part of the work contained herein has been submitted to any other university or place of learning for any degree, diploma or other qualification. The work is intended to be submitted to the Jounral of Fluid Mechanics, or Physics of Fluids.

Acknowledgements

It is with my sincerest gratefulness and warmest regards that I dedicate this work to my family and friends. Growing in a traveling household was a challenge as a child but it was an opportunity that I have grown to appreciate day by day. I would like to thank my parents, Kyaw Tun Wai and Moe Thuzar for raising me and giving me that opportunity to see the world. I would also like to mention my two brothers, Myat Thurein and Aung Thukha for their love and support.

I would also like to mention my friends who kept me motivated during challenging times. I would like to thank my fellow graduate students, Iman Bahreini, Amir Gharavi, Mohammad Ghazizadeh, Saeideh Kheradmand, Arman Rokzhadi, and Xiaohui Yan, whose hard work, intellect and open-mindedness has inspired me so much. I am also moved by the care, support and kindness of Rufino Ansara, Leia Atkinson, Nicholas Laroux, Yoko Kawaguchi, Leila Mouhsine, and Sahra Nur. I truly feel that friends are the family that you choose. I am eternally grateful for your company.

Last, but not least, I would like to thank my supervisor, Dr, Abdolmajid Mohammadian for sharing his knowledge and expertise to guide me through this process. His disposition for mathematical sciences and analytics always amazed me. I am grateful that he has persisted to support my studies, even in the uncertain times of my stay in Canada.

Contents

List of Figures

List of Tables

Nomenclature

$\bar{\phi}$	amplitude of the perturbation
κ	condition number
$\mathbf{V}$	matrix whose column vectors are the eigenvector
$\overline{S}$	bed friction number at the inflection point
ϕ'	generic representation for a perturbation
A	matrix A in the generalized eigenvalue problem
B	matrix B in the generalized eigenvalue problem
C	operator matrix
c	temporal frequency
c_f	friction cofficient
D	Chebyshev differentiation matrix
h	flow depth
k	wavenumber
N	number of nodes in the computational domain
P	mean pressure

p	pressure
p'	pressure perturbation
S	bottom friction stability parameter/bed friction number
$sech$	hyperbolic secant function
$tanh$	hyperbolic tangent function
U	base flow velocity
u	velocity in the streamwise direction
u'	velocity perturbation in the streamwise direction
U_a	ambient velocity parameter
v	velocity in the cross-stream direction
v'	velocity perturbation in the cross-stream direction
x	coordinate in the streamwise direction
y	coordinate in the cross-stream direction

Chapter 1

Introduction

Turbulence, the chaotic motion in fluid flows, has been a subject of interest for centuries, yet much of it is still not well understood. In fact, it is one of the unsolved problems of physics worthy of a millennium prize. The phenomenon of turbulence has been recognized since the 1500s by the famous polymath Leonardo da Vinci whose description of it was (Drazin and Reid, 2004):

> "...the smallest eddies are almost numberless, and large things are rotated only by large eddies and not by small ones, and small things are turned by small eddies and large "

This description along with his sketch as shown in figure 1.1, is a very accurate description of turbulence and its coherent structures such as eddies, whirlpools or vortices. The term turbulence was perhaps coined by " turbolenza" which da Vinci used to refer to the phenomenon.

Fluid instability is the tendency of the flow to become turbulent and will be a major point in this thesis. The theory of hydrodynamic stability will be elaborated further in the following section. The focus of this thesis is on shallow flows, and particularly on the use of stability theory in describing the generation of coherent structures, such as whirlpools or vortices. Following a brief introduction of " shallow flows" with examples thereof, this chapter describes these turbulent structures, their life cycle, the ways in which they have

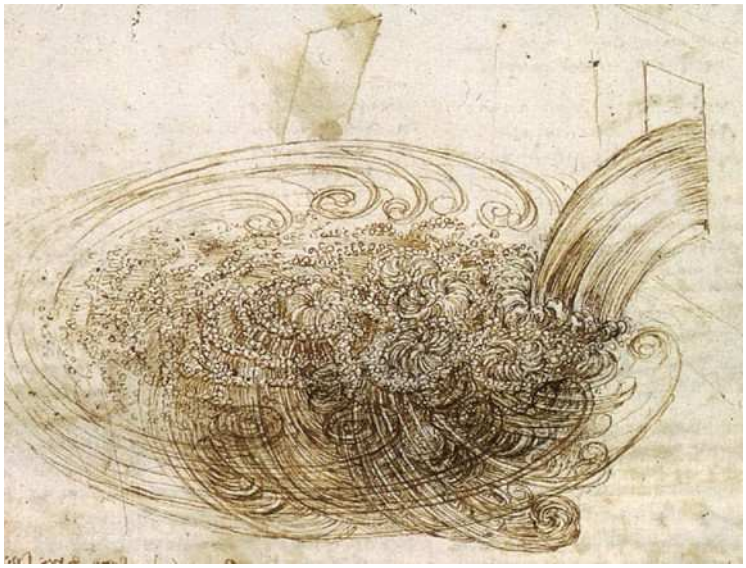

Figure 1.1: A sketch by Leonardo da Vinci showing a fluid flow with characteristics of turbulence

been investigated to date, and the current theory with respect to how they behave, and concludes by defining the research question, objectives and scope of work undertaken to expand upon and further demonstrate this theory.

1.1 Hydrodynamic Stability Theory

Hydrodynamic stability theory is traditionally seen as the study of how laminar fluid flows transition into turbulent flow. The theory is highly mathematical in nature and deals with dynamical systems, which are systems with dependence on time and space. Examples include swinging of a pendulum or the flow of water in a pipe. A dynamical system is said to be stable if it is able to return to its equilibrium state after being perturbed. The concept of stability can easily be demonstrated by the "ball in a trough" example as shown in figure 1.2.

System (a) (figure 1.2a) is stable because if the ball is perturbed or moved, it will always return to the bottom of the trough, which is the equilibrium state. On the other hand, system (b) (figure 1.2b) is unstable because any movement of the ball will alter the system

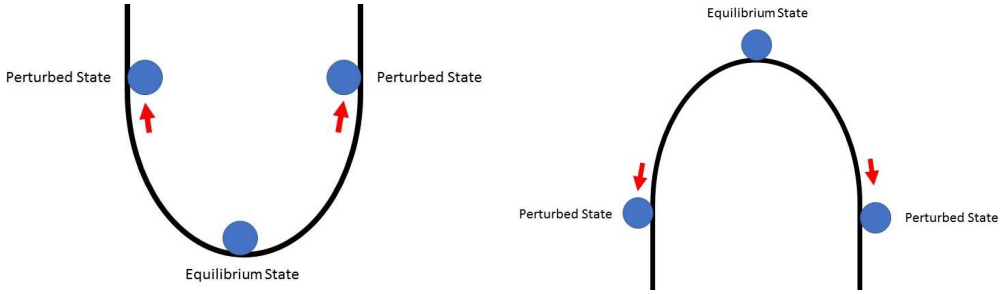

(a) A stable system (b) An unstable system

Figure 1.2: Stability of a dynamical system

permanently and the system will not return to its equilibrium state naturally.

In terms of fluid flows, stability can be seen as the sensitivity to perturbation of the flow variables. In a stable flow, if we take a laminar flow of an arbitrary fluid, and perturb the flow field (i.e. the velocities), the perturbations will eventually decay and the flow will return to its original laminar state (figure 1.3a). On the other hand, an unstable flow would react to the perturbations by amplifying them and changing the flow dynamics permanently, resulting in chaotic motion and vortices (figure 1.3b).

The beginning of hydrodynamic stability theory can be attributed to a series of experiments conducted by Reynolds (1883). The use of the Reynold's number in modern turbulent flow models can be traced to these experiments. The field of study has since undergone many developments including the formulation of the stability problem for viscous parallel flows by Orr (1907) and Sommerfeld (1908),which resulted in the famous Orr-Sommerfeld equation, the inviscid modified form (Rayleigh's equation) of which is derived in Chapter 3.

Major efforts in hydrodynamic stability theory went into linear stability analysis or eigenvalue analysis, in which the linearized equations are analyzed for growth or decay of perturbations. This so-called modal analysis, although reasonably useful and widely done, has its limitations. Trefethen et al. (1993) introduced the concept of pseudospectra or pseudo-eigenvalues. It is well established that the critical Reynold's number predicted by linear stability analysis does not match experimental values. This discrepancy is often attributed to the linearization process but Trefethen et al. (1993) stated that it may be coming from

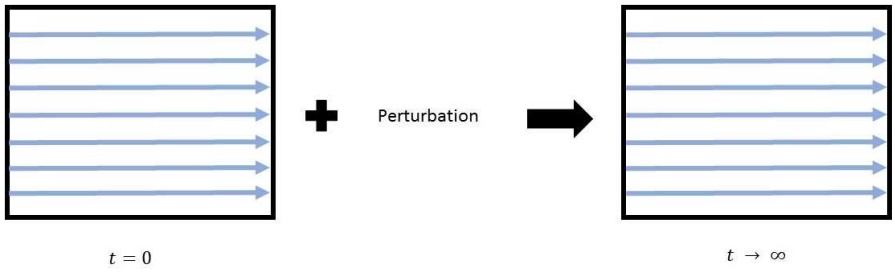

(a) A stable flow

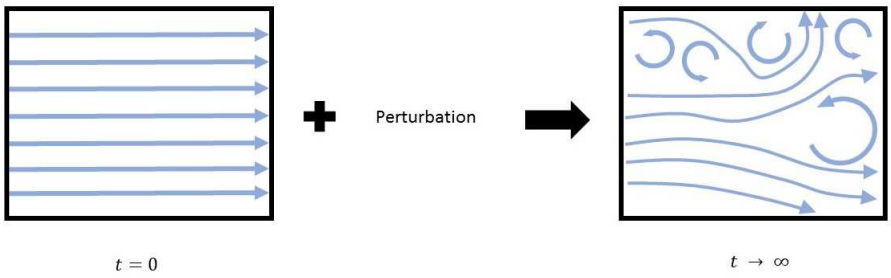

(b) An unstable flow

Figure 1.3: Stability of fluid flows

the nonnormality of the linear operator propagating the solution in time. Later, a comprehensive paper by Schmid (2007) about a nonmodal stability analysis uses energy growth and concluded that linear stability analysis is only a prediction of asymptotic stability. A more in-depth description of nonmodal stability is given in a later chapter.

1.2 What are Shallow Flows ?

Before we embark on examining the core problems associated with instability of shallow flows, it is important to clarify the notions of " deepness " or " shallowness " of a water body. Contrary to everyday use, where the term " shallow " is taken in an absolute sense to mean water less than a metre or so in depth, when used in a technical sense in fluid dynamics, it refers to the characteristic of having a much larger width than depth, whatever that depth may be. In other words, the ratio of depth to width of a shallow flow is less than one.

A more generalized technical definition given by Uijttewaal and Jirka (2004) describes shallow flows as "bounded, layered turbulent flows in a domain for which two dimensions, namely the dimension in the direction of the flow as well as one transverse dimension, greatly exceed the third dimension."

Therefore, it becomes evident that the concept of "shallow water" and its inherent assumptions are important in many geophysical and environmental applications, such as hydrodynamic modelling of flood events. Figure 1.4 shows a simple schematic of a shallow flow.

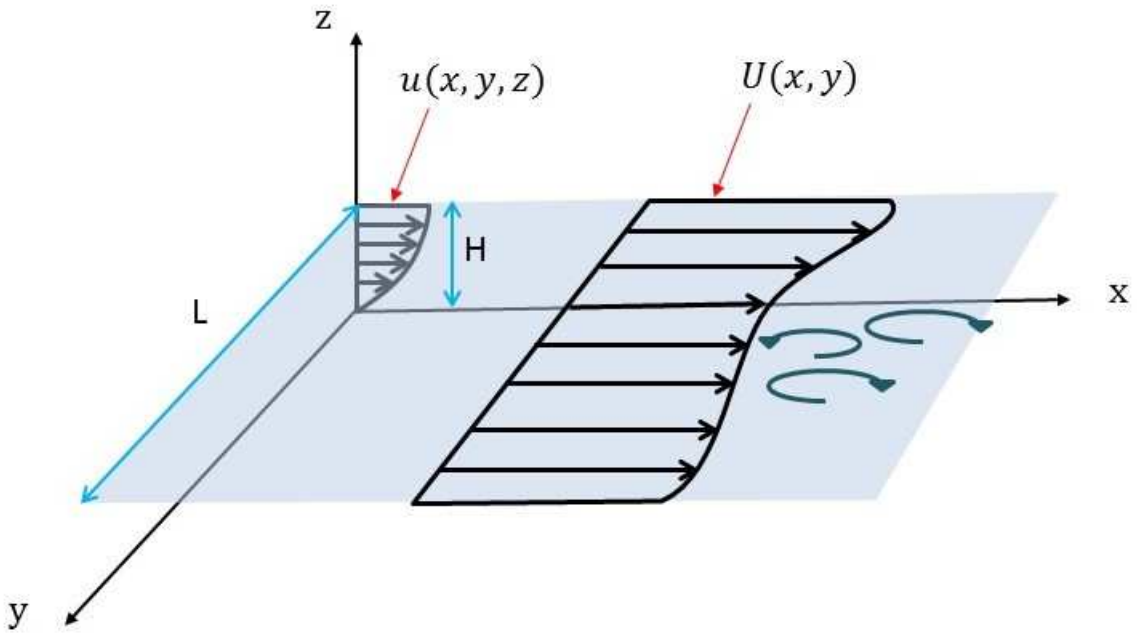

Figure 1.4: A typical shallow flow

Mathematically, the ratio of the flow's height or depth, H, to its horizontal (transverse) length, L, is less than 1 for shallow flows. In the shallow flow given in figure 1.4, in which the fluid is moving along the *x-axis*, both this dimension and the transverse dimension L greatly exceed the third dimension H. The parallel flow assumption is adopted in this thesis and thus only the streamwise velocity u, the velocity component parallel to the overall flow, is considered, making the flow unidirectional. The vertical velocity profile at point (x, y) is denoted by $u(x, y, z)$, shown here as a logarithmic profile at the boundary. Bed

shear, caused by the interaction of the flow with the bottom boundary, produces ejection and sweep motions in the fluid, which results in hairpin-shaped loops of fluid motion called hairpin vortices. The growth of these three-dimensional structures, however, are confined to the depth of the flow. By depth averaging the vertical velocity profile across the channel, the transverse velocity profile $U(x, y)$ representing the baseflow, a simplified representation of the three-dimensional turbulent flow, is obtained. Two-dimensional coherent structures, to be discussed in detail in Chapter 2, are depicted as vortices in dark blue in figure 1.4. Often, the variation of streamwise velocity across the channel produces transverse shearing of the fluid layers. An inflexion point in the velocity profile is a necessary condition for instability. The turbulent base flow that was described is sensitive to disturbances (unstable) and may produce oscillations in the lateral direction which in turn may produce large scale coherent structures. Since the length scale in the lateral direction is much larger, these coherent structures are two dimensional or quasi-two-dimensional and can be significantly large, contributing to transverse exchange of momentum and mixing.

1.3 Shallow Flows Around Us

Shallow flows are ubiquitous in our surroundings, not only present in natural settings but also in technological applications.

Rivers, streams and creeks, with their often large width-to-depth ratio, are considered unidirectional shallow flows. The topography through which they flow, around irregular terrain and over uneven surfaces with features such as islands, or bridge piers, leads to the development of large vortices in these flows. These vortices contribute to the exchange of mass and momentum of the water itself and both macroscopic and dissolved contents in the lateral direction and greatly influence the movement and deposition of sediments such as the formation of sediment deposits at the river mouth called mouth bars. Figure 1.5 shows the Irrawady River in Myanmar, an example of a shallow river.

Similarly, although we may often consider them to be still in comparison to rivers, lakes

Figure 1.5: The Irrawady River, Myanmar

are actually quite dynamic, driven by many sources of forcing by nature. Circulation in lakes induced by thermal stratification, creating buoyancy differences, is a result of receiving energy from the sun. Wind shear at the surface and also the inflow of rivers and creeks into the lake also creates motion in lakes. These dynamics can be explained in the shallow flow framework.

The ocean and the atmosphere, which are normally considered deep, are technically a shallow system since it is a thin layer of fluid relative to the surface area of the earth it envelops. The ocean is highly stratified, which give rise to shallow dynamics within the stratified layers and also as a whole (Uijttewaal and Jirka, 2004). The atmosphere may also be governed by shallow dynamics for the entire depth scale or that of each stratified layer, with strong interactions with the mountain topography (Uijttewaal and Jirka, 2004). Figure 1.6a shows the ocean with large vortical structures that fit in the shallow water dynamics. A view of the atmosphere from space is shown in figure 1.6b to help conceptualize it as a shallow fluid layer.

However, not all oceanic and atmospheric phenomena can be modelled using shallow water dynamics. Only large scale processes whose length scale is much larger than the ocean or atmosphere itself can be accurately captured using shallow water assumptions.

Many mechanical components in household electronics, automobile and other technology also display shallow flow characteristics. Examples include cooling systems such as air conditioners (flat plenums or distribution chambers) or heating systems such as hot water

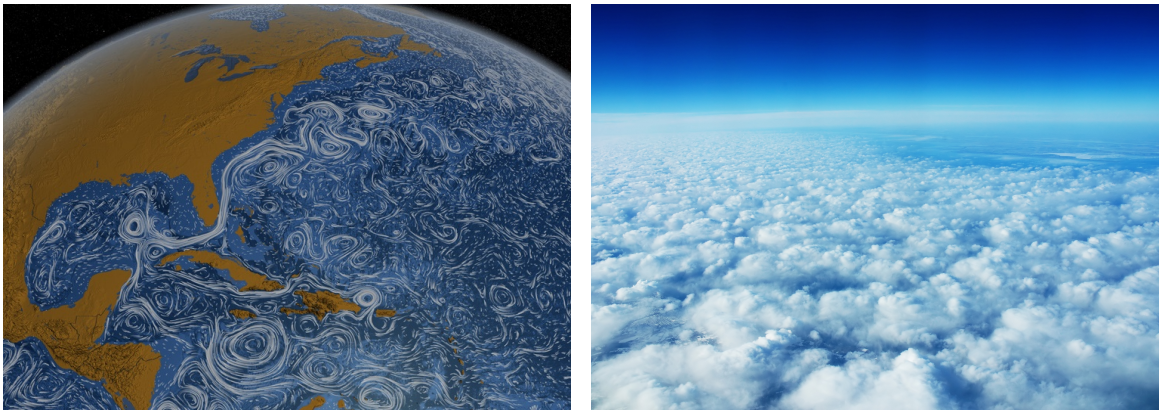

(a) Oceanic eddies (NASA) (b) View of the atmosphere from space (NOAA)

Figure 1.6: Shallow fluid systems not commonly conceptualized as such

heaters (plate heat exchangers). They can also be observed in manufacturing of products such as sheet metal (liquid metal sheet casting processes).

1.4 Two-dimensional Coherent Structures

Uijttewaal and Jirka (2004) defined Two-Dimensional Coherent Structures (2DCSs) as "connected, large-scale turbulent fluid masses that extend uniformly over the full water [or other fluids] depth and contain a phase-correlated vorticity, with the exception of a thin near-bottom boundary layer," an adapted version of the more general definition for three-dimensional coherent structures given by Hussain (1983). These structures tend to be generated by means of three mechanisms, then grow larger and eventually decay.

The mechanisms of 2DCS generation are scientifically undisputed. Listed from strongest to weakest, they are as follows: (1) topological forcing, (2) internal transverse shear and (3) secondary instabilities (Jirka, 2001).

Topographic forcing occurs when a flowing fluid, such as a river, interacts with large topographical features such as islands, sand bars, and man-made structures. When the flow hits the topographic feature, the fluid begins to separate, and a shallow wake is formed behind the feature. This results in what is referred to as transverse shearing in the streamwise

velocity profile downstream of the topography, which results in instabilities which grow into 2DCS.

Internal transverse shear is said to create 2DCSs when the streamwise velocity of the flowing fluid varies across the channel through which it is flowing. This transverse shear velocity profile may be a consequence of different sources of inflow carrying different energy and momentum or the gradual change of bathymetry and roughness.

The third and weakest mode of generation is due to secondary instabilities, caused by the imbalance of the equilibrium between the three-dimensional turbulence production and dissipation. Relative to the first two means of generation, very little information on the formation of 2DCSs out of secondary instabilities has been reported to date in the literature.

Once generated, 2DCSs tend to grow and develop into larger vortical structures and eventually decay with the dissipation of their energy. Growth of the vortical structures of the 2DCSs is by means of entrainment or engulfment by external fluid that is less turbulent. Smaller coherent structures can also merge together and form larger 2DCSs.

When the energy driving the 2DCSs dissipate, they eventually decay. In three-dimensional turbulence, the energy is transferred from large scale to small scale. In other words, larger vortices have greater energy, which breaks down into smaller and smaller vortices until viscosity is responsible for the dissipation of energy rather than the momentum of the motion itself. However, in two-dimensional structures, the reverse is true. Smaller vortices feed energy to the larger eddies. In this sense, two-dimensional turbulence is more long lived and viscosity obviously is not responsible for dissipating energy of large scale structures. The major mechanism through which 2DCSs lose their driving energy is their interaction with the channel bed, or namely bed friction.

1.5 Methods of Investigation

Researchers studied the behaviour of 2DCS, from generation to growth and decay, empirically through experimental studies, computationally through numerical simulations and theoret-

ically through stability analyses. These studies are seen to focus on three general cases of shallow flows; shallow jets, wakes and mixing layers which are discussed further in Chapter 2.

Traditionally, empirical experiments are performed in an artificial water channel called a flume. To visualize the otherwise indiscernible coherent structures, a coloured dye is injected into the water. Recent developments in laboratory techniques such as particle image velocimetry (PIV) and laser induced florescence (LIF) enable researchers to improve not only their measurements of these structures, but also their visualization. In these techniques, the flow is injected with reflective particles while a laser beam or sheet is projected into the water. Specialized cameras are then mounted and calibrated to take images that can be processed into a flow field.

On the computational side, numerical simulations can be used to simulate experiments in a virtual environment. With the development of more advanced computational tools and more reliable numerical models, numerical simulations are widely used. Also, large scale phenomena in the ocean and atmosphere can not be modelled to full scale in the laboratory environment and hence numerical simulations are used in such settings.

Linear Stability Analysis (LSA), the subject of the present investigation, is a theoretical approach to understanding the development of 2DCSs through the instability of the fluid itself. As defined in section 1.1, an unstable flow is one in which added perturbations tend to grow and change the flow dynamics from the original state. For a dynamical system describing fluid flow, LSA is conducted by adding infinitesimal perturbations to the flow variables around the base flow. This yields a linear system of differential equations describing the evolution of the perturbations. According to the Fourier transform, any function can be represented as a summation of waves and thus the perturbations are assumed to be waves or a combination of waves. The result is an eigenvalue problem which takes the form of an Orr-Sommerfeld equation. The growth rate of each wave component of the perturbation can be obtained from the eigenvalues. Although some limitations, discussed further in Chapter 2, may exist, it has been applied with reasonable success by many authors.

In this thesis, a further development in linear stability theory called nonmodal stability is used. It is done as an extension to the conventional linear stability or eigenvalue analysis. A detailed description of the method is described in Chapter 3.

1.6 Statement of Research, Objectives and Scope

Chapter 1 has been dedicated to give the reader a background of shallow flows, their omnipresence in nature, and the life cycle of 2D turbulent coherent structures. As mentioned above, the use of linear stability analysis is prominently featured in the study of shallow flows, although its limitations in describing shear driven flows are reported in literature.

The main objective of this thesis is to analyse the stability of shallow flows in finite time. The scope of the study as as follows:

1. Conduct a traditional linear modal stability analysis to obtain the critical cases.
2. Evaluate the critical cases for potential of nonmodal behaviour.
3. Compute the transient evolution of energy for the critical cases.
4. Justify the need for nonmodal stability through nonnormality of the operator.
5. Generalize the results of the nonmodal analysis in the relevant parameter space.

1.7 Overview of the Chapters

The thesis is organized into six chapters. Chapter 2 presents the literature available on the subject of shallow flows and their hydrodynamic behaviour. The chapter also reviews the method of nonmodal stability and the literature on why it may be needed in addition to modal stability for some flows. Chapter 3 introduces the readers to the methodology of analysis. The governing equations are presented, followed by the numerical solution methods, parameters of interests and other assumptions and derivations. The details and

definitions for both linear modal and nonmodal analyse are given in this chapter. The details of the results are then given in chapters 4 and 5. Chapter 4 revisits the traditional linear modal analysis method to obtain the critical cases and takes a step further to evaluate the potential for nonmodal behaviour as explained in Chapter 3. The chapter concludes by presenting the transient amplification of energy in time for the critical cases obtained using the modal analysis, cementing the importance of nonmodal analysis. Further results are given in Chapter 5 which further justifies the need for nonmodal analysis using the nonnormality of the matrix operators in shallow flows. Then, the nonmodal stability regions are presented to complete the picture of finite time behaviour for shallow flows. The thesis is then concluded in Chapter 6 with the summary of the results, recommendations and potential expansions to the research in the future.

Chapter 2

Literature Review

Shallow flows have been studied by means of experiments, numerical simulations and stability analyses. The current chapter presents the various work performed by researchers to better understand the instability of shallow flows and its impact on flow behaviour. The limitations of the linear modal stability itself is also presented with an accompanying introduction to a proposed newer method.

The generation of large scale coherent structures in shallow flows in literature is represented by three main cases, namely shallow wakes, shallow jets and shallow mixing layers. In the case of a shallow wake, an obstacle (e.g. islands, bridge piers) is present in the flow which causes flow separation, resulting in a shearing velocity profile downstream of the obstacle. Figure 2.1c [1] shows a satellite image showing the wakes behind islands. On the other hand, jets (e.g. waste water and industrial discharges, river flowing into the sea) are discharges into a waterbody and act as a source of velocity and momentum which creates a shearing velocity profile almost the exact opposite of a shallow wake. The discharge of the Grand Haven river in Michigan is shown in figure 2.1b [2] where the river plume is visible due to the sediment content. The last case is a shallow mixing layer, which is caused by the transverse shear generated from differential streamwise velocity. An example of this would be a confluence

[1] $https://directory.eoportal.org/web/eoportal/satellite-missions/t/terra$

[2] $https://wmeac.org/enormous-grand-haven-plume-shows-impact-of-increased-stormwater-runoff/$

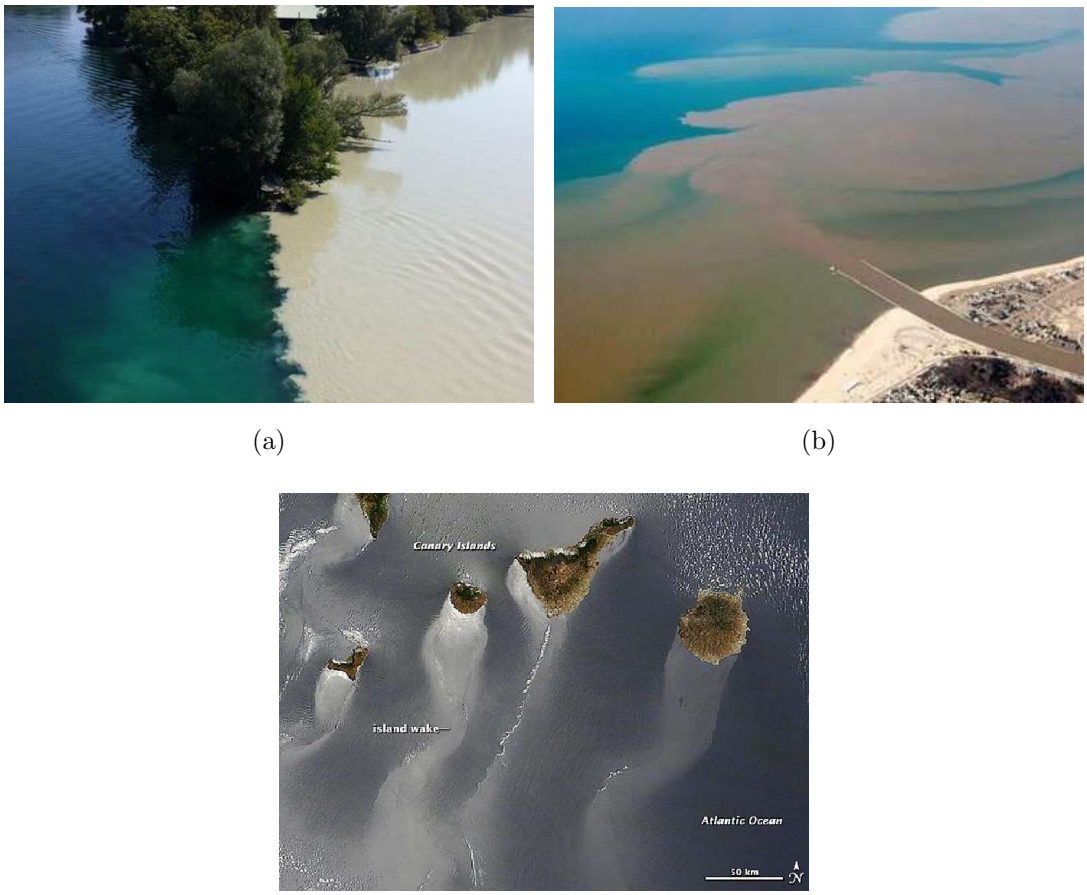

(a) (b)

(c)

Figure 2.1: Shallow flows in nature (a) a confluence of two rivers with different sediment content[3], (b) a high sediment content river discharging into the sea[2], (c) wakes behind islands[1]

of two rivers, such as that of the Rhone and Arve Rivers in Geneva as shown in figure 2.1a [3]. In all cases, inflexion points can be observed in the velocity profile and instability can be expected. Many studies have been conducted to evaluate the conditions of instability in these cases.

Figure 2.2 visually represents the linear stability analysis procedure for shallow flows, showing the associated velocity profile for each case and the generation of 2DCSs as a result of growing perturbations.

[3] $http://twistedsifter.com/2012/04/confluences-around-the-world/$

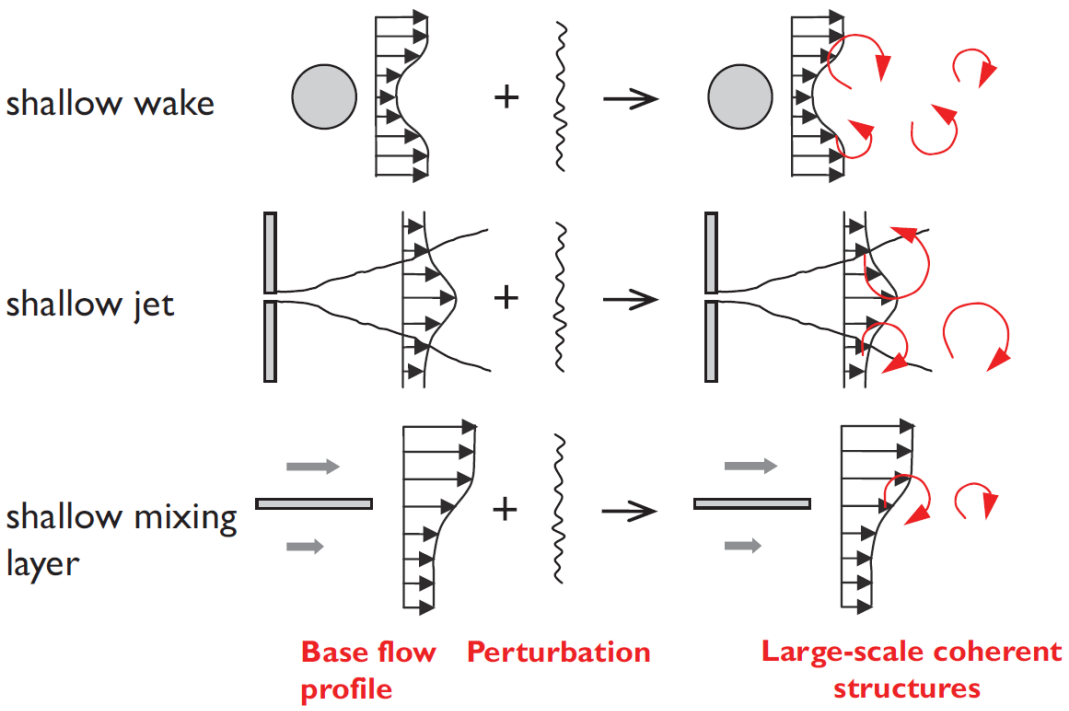

Figure 2.2: The development of coherent structures in shallow flows from perturbations (Ghidaoui et al., 2012)

Jets exhibit Gaussian-like velocity profile with the highest velocity at the source. Strong self-similarity is observed from measurements done in laboratory experiments by Jirka (2001) and using this self-similarity assumption, the shallow jet profile as a hyperbolic secant function can be readily derived from the Navier-Stokes equations Chen and Jirka (1998).

As for wakes, laboratory measurements Carmer et al. (2001) and Socolofsky et al. (2004) show that the self-similarity assumption is valid for far-wake profiles. In near-wake regions, the jet-like features appear on either side of the wake profile, which introduces additional inflection points and thus increase the instability. However, strong recirculation was present and its effect is greater than that of the additional inflection point. Therefore, a hyperbolic secant function is also a valid representation of the wake profile. Contrary to the jet, a wake exhibits a Gaussian-like velocity profile with a trough rather than a peak.

Unlike jets and wakes, the mixing layer profile is made of two velocity plateaus, one

higher than the other and a transition region. Experimental studies were conducted by van Prooijen and Uijttewaal (2002) and their measurements concluded that the hyperbolic tangent function is a suitable representation of a mixing layer velocity profile.

2.1 Shallow Jets

Jets are created when a higher velocity fluid is projected into a larger flow with an ambient velocity. Many types of jets exist but the current review focuses on parallel shallow jets, for which the effect of viscosity is minimum and thus controlled mainly by bed friction Chen and Jirka (1999) . The hydrodynamic behaviour of shallow jets has been studied in detail in experimental settings by Dracos et al. (1992) and Chen and Jirka (1999).

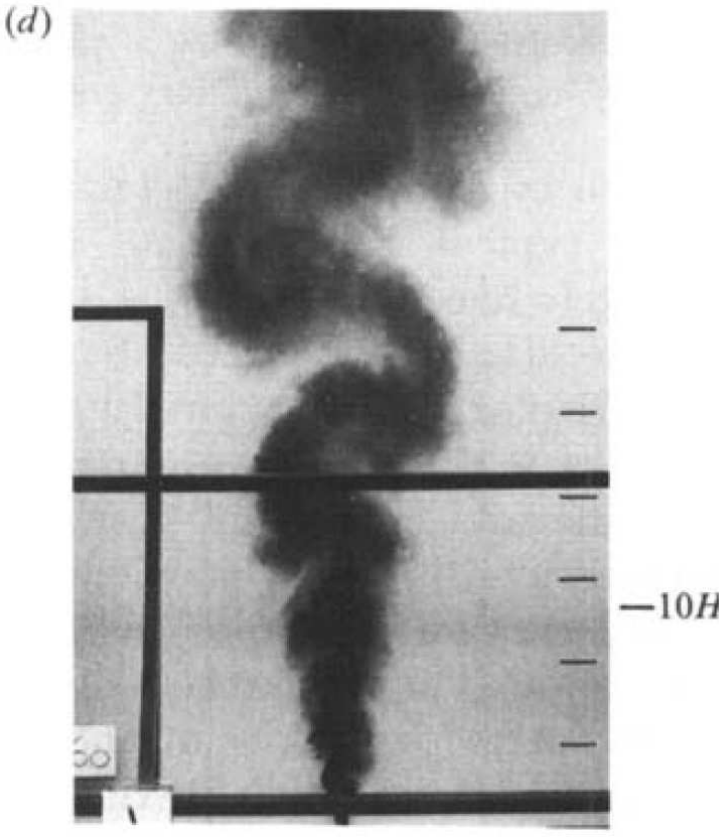

Figure 2.3: Shallow jet in an experimental study (Dracos et al., 1992)

Figure 2.2 shows a shallow jet in the experiments by Dracos et al. (1992). The region

immediately after the discharge of the jet into the ambient water body is called the near field, which extends till twice the width of the discharge itself. In the near field, the flow behaves like a classical two-dimensional jet. The mid-field extends from the end of the near field to ten times the width of the discharge. At this stage, secondary currents occur and affect the jet over the flow depth. Finally, the far field is the zone at a distance greater than 10 times the depth of the flow. It is in the far field that the jet begins to exhibit meandering and large scale two-dimensional vortices (Dracos et al., 1992).

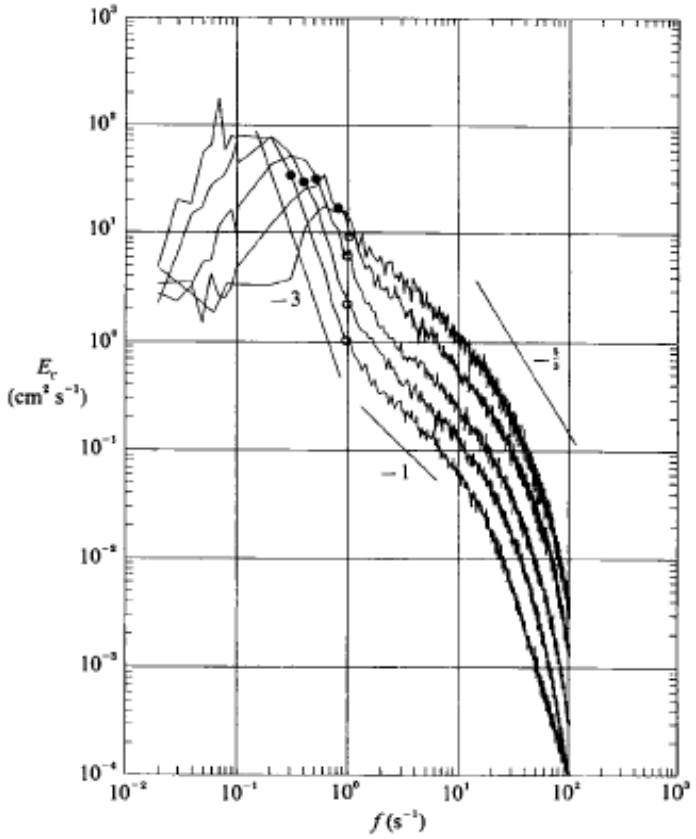

Figure 2.4: One dimensional energy spectra of a jet, showing a region of −3 slope (Dracos et al., 1992)

The presence of two dimensional vortices can also be seen in the energy spectrum computed from the time records of velocity given by Dracos et al. (1992) shown in figure 2.4. The maxima of the energy density in the middle field is found to be constant while in the far field, the peak around the maximum is more pronounced. An additional range also de-

velops in the far field where a -3 wavenumber dependency on the spectra is observed. This dependency is reported to be correlated to the observance of two-dimensional turbulence (Batchelor, 1969).

Earlier work on Linear Stability Analysis (LSA) using the inviscid Rayleigh problem established the stabilizing effect of bed friction. Chu et al. (1991) is one of the pioneering works in parametrizing the effect of bed friction into a non-dimensional number S, which is subsequently used by many following studies. The effect of viscosity or lack thereof to the stability domain (Chen and Jirka, 1999) is further elaborated by Ghidaoui and Kolyshkin (1999) which stated that for flows with Reynold's number higher than 1000, its effect is minimum.

Further linear stability work is done by Socolofsky and Jirka (2004) which evaluated the spatio-temporal stability of shallow flows. The velocity ratio parameter R was defined which determines whether the jet is discharging into a stagnant waterbody ($R = 1$), a counter-flowing waterbody ($R > 1$) or a co-flowing waterbody ($R < 1$). Evaluating R and the spatio-temporal growth rates in terms of the bed friction number revealed that only convective instabilities, ones which are convected in the direction of the flow, are present. With higher R, higher bed friction is needed to stabilize the flow.

2.2 Shallow Mixing Layers

When a fluid flow consists of zones where the velocity is different, a mixing layer is formed at their interfaces. The transverse shear causes the instabilities in the mixing layers and forms large 2DCSs. Shallow water mixing layers are strongly affected by bed friction which diminishes the difference in velocity and promotes the growth of the mixing layer width (Uijttewaal and Booij, 2000). The growth of the mixing layer width is attributed to the development of 2DCSs and their merging and paring (Chu and Babarutsi, 1988). Browand and Troutt (1980) report the correlation between the growth of the length scale of spanwise vortices to that of the width of the mixing layer.

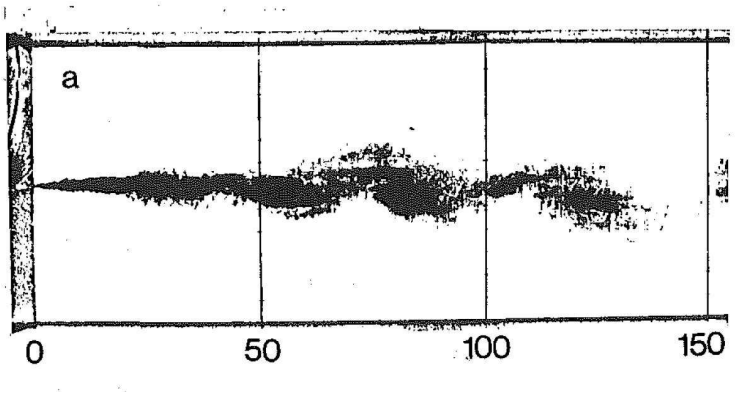

(a)

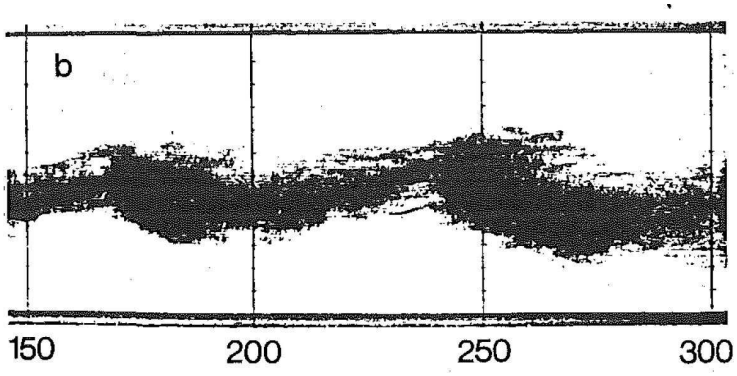

(b)

Figure 2.5: Mixing layers in an experiment (Chu and Babarutsi, 1988)

A numerical model presented by Ghidaoui and Liang (2008) describes the behaviour and the development of the mixing layer, stating that the formation of Kelvin-Helmholtz instabilities is initiated at the splitter plate where the flows of two different velocities meet. These instabilities travel downstream and form vortices by rolling up. Paring of these vortices result in 2DCSs further downstream. Mixing layers are highly sensitive to perturbations at the inflow boundary (Ghidaoui and Liang, 2008).

The development of the mixing layer and the applicability of linear stability is brilliantly summarized by Ghidaoui et al. (2012). Three different zones, similar to that of the jet, can be identified in a mixing layer as well. The region close to the inflow boundary, where the mixing layer behaves like a plane wave is the plane wave region. Further downstream, the plane waves start to oscillate more and the transition zone, where the vortices start forming,

begins. Finally, the last region is that of vortex merging.

The spectra of the numerical experiment by Ghidaoui et al. (2006) is presented in Ghidaoui et al. (2012) and is compared to the linear stability analysis results give in Chu et al. (1991) and Ghidaoui and Kolyshkin (1999). The dominant modes can be computed from the velocity spectra and it is shown from observing the spectra at different locations that the range of unstable frequencies and the most unstable mode obtained from linear stability analysis are in agreement. It is seen that linear stability is able to accurately predict the growth of certain wave components of the perturbation, only in the plane wave region.

2.3 Shallow Wakes

Shallow wakes are formed when a topographical feature, an island or a bridge pier, partially obstructs the flow. A separation zone is formed behind the feature, which causes turbulence and a transverse shear in the mean flow, consistent with type A generation of 2DCSs described in Chapter 1.

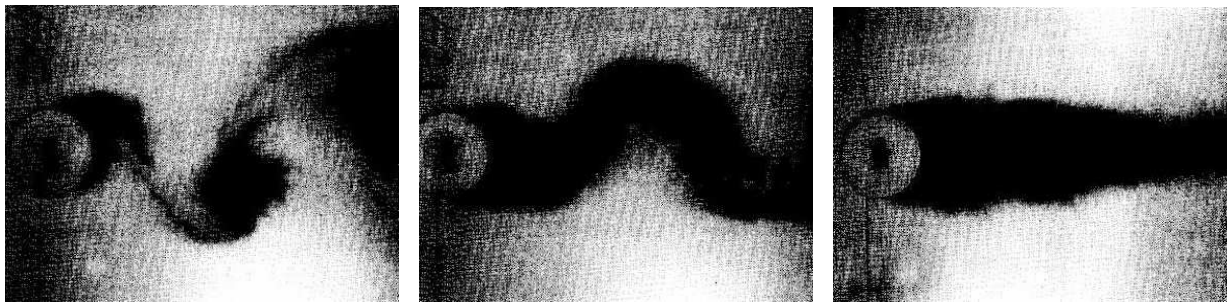

(a) Vortex Sheet (b) Unsteady Bubble (c) Steady Bubble

Figure 2.6: Shallow wake under different regimes (Chen and Jirka, 1995)

Experimental studies were done by Chen and Jirka (1995) to evaluate wakes. In particular, the wake behind a cylinder is seen to exhibit three distinct flow patterns dependent on the bed friction number and not Reynold's number. One of them is called vortex sheet (VS) which is characterized by a pronounced vortex shedding mechanism at the near-wake. It is seen that the wake has a fuzzy and streaky appearance, caused by small scale turbulent mix-

ing, which is in turn caused by bottom friction and lateral instabilities. The wake is largely two-dimensional, with three-dimensional turbulence occurring weakly in the thin bottom boundary layer only. The second type of flow patter found is unsteady bubble (UB), which is characterized by a bubble attached and recirculation at the near-wake, but no vortex shedding. Transverse disturbances grow downstream as the bubble becomes unstable. Lastly, the steady bubble (SB) flow pattern occurs when the attached bubble and recirculation zone extends downstream and the wake is stable without instabilities.

A major contribution to the shallow wakes and also to all shallow flows is the work by Chen and Jirka (1997), in which spatio-temporal stability of wakes is related to the flow regimes described earlier. A fluid is absolutely unstable if the perturbations grow in both upstream and downstream directions, contaminating the entire flow. In contrast, convective instabilities are perturbations which are swept away from the source as they grow (Huerre and Monkewitz, 1990). Chen and Jirka (1997) identified branch point singularity of the inviscid dispersion relationship, reported by Betchov and Criminale Jr (1966) to identify the presence of absolute instabilities.

The transition bed friction numbers from absolutely to convectively unstable states of a wake flow are calculated using impulse response and Green's function. A very important contribution of this work by (Chen and Jirka, 1997) is that the transition bed friction numbers between absolute and convective instabilities also signified the transition between VS, UB and SB flow patterns observed in Chen and Jirka (1995). Linear stability of the spatio-temporal behaviour represented the flow patterns and their transition very well.

2.4 Limitations of the Modal Stability Approach

As mentioned above, many publications on linear stability of shallow flows are available in literature and they are reasonably in agreement with experimental and numerical studies. However, the inability of linear stability analysis in accurately predicting the Reynold's number for transition is well documented and summarized in Trefethen et al. (1993) and Schmid

(2007). While linear stability analysis gives results that perfectly agree with experiments for thermal and centrifugal problems such as Rayleigh-Bénard convection, significant discrepancies can be seen in shear driven flows such as Poiseuille and Couette flows shown in figure 2.7 (Trefethen et al., 1993). The plane Poiseuille flow is used below to describe the limitation of linear stability.

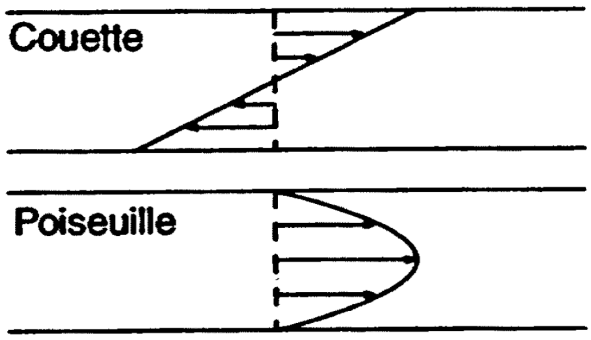

Figure 2.7: Shear flows (Trefethen et al., 1993)

A number of studies reported the Reynold's number at which the plane Poiseuille flow transitions from laminar to turbulent flow called the critical Reynold's number. This is done by conducting a linear stability analysis, usually results in the Orr-Sommerfeld equation. Orszag (1971) used the Chebyshev spectral method on the Orr-Sommerfeld equation and determined the Re_{cr} to be 5772.22. Similar results were also seen using finite different methods, such as Thomas (1953) which reported 5780 and Nachtsheim (1964) which reported 5767. Shen (2012) used asymptotic methods described in Lin (1955) and reported the value of 5360. Orthogonal function expansions were also used by Grosch and Salwen (1975) and reported 5750. From all these linear stability studies, it can be said that there is a reasonable agreement amongst them that the critical Reynold's number was around 5000 to 6000.

Experimental studies were done by Patel and Head (1969) in which a rectangular parallel sided channel. The transition to turbulence were evaluated in terms of the relationship between skin friction and Reynolds number, the applicability of log law in the regions near the wall. The study reports that the transition Reynold's number ranges from 1350 to 2500 and 3000. These values are clearly not in agreement with the values obtained from linear

stability analysis.

Discrepancies between linear stability analysis can also be found in Couette flows. Although, they are not presented here, the studies using linear stability can be found in Herron (1991) and experimental studies can be found in Lundbladh and Johansson (1991) and (Tillmark and Alfredsson, 1992).

2.5 Nonmodal Stability Theory

The linear stability analysis in hydrodynamic stability can be described in two parts. The first part is the linearization process in which the system is linearized about a basic state and the second part is finding the unstable eigenvalues of the linearized system. The discrepancies described in the previous section are traditionally attributed to the first part. Thus, the linearization itself is seen as contributing to the error and so the focus has shifted towards looking at nonlinearities more closely (Trefethen et al., 1993).

However, there is another approach to linear stability analysis from a different perspective. The traditional method is based on eigenvalues, and identifying the fastest growing mode, hence the term modal analysis. If the fastest growing mode grows exponentially, the system is deemed unstable. It is pointed out in Reddy and Henningson (1993) and Trefethen et al. (1993) that this approach is not sufficient when the linear operator which propagates the solutions forward in time is non-normal. The linear operator, which is a matrix, is normal if the set of all its eigenvectors are orthogonal to one another. It is pointed out that in the case of Poiseuille and Couette flows, the linear operators are not normal Reddy and Henningson (1993) and Trefethen et al. (1993). In fact, nonnormality of the linear operator can be seen in many shear flows and it is often the case. The energy in the perturbations can grow significantly in the case of nonnormal operators. Traditional linear modal stability analysis is therefore only indicative of asymptotic stability and gives no insight into growth in finite time. The modal approach can be replaced with a nonmodal stability analysis which considers and initial value problem, instead of an eigenvalue problem.

In nonmodal analysis, the aim is to capture the behaviour of the perturbation, i.e. the energy it contains, in a finite-time horizon. In the analysis of finite-time stability, the perturbation that contains the most energy in short timescales is different from the most unstable mode, and thus markedly deviates from the Lyapunov stability concept (Khalil, 2002). Nonmodal stability theory covers both the response of a perturbed initial condition or external forcing (Schmid, 2007). The scope of this current thesis covers the response to initial condition evaluated by means of various metrics indicative of nonmodal instability and lower bounds to the maximum energy growth (Schmid, 2007). The maximum energy growth optimized over all initial conditions over time can also be calculated, which in turn can be used to calculate the optimal initial condition (Schmid, 2007).

Conveniently, Schmid (2007) presented the nonmodal stability theory in terms of Poiseuille flow, which nicely ties together the discrepancy in the prediction of critical Reynold's number by LSA and by experiments as mentioned in the previous section. One of the concepts to consider in nonmodal stability is pseudospectra or pseudo-eigenvalues. Simply put, they are contour lines around the spectra or the set of eigenvalues that gives the extent of change the spectra can experience under perturbations of certain orders. Another metric is called the numerical abscissa, corresponding to the slope of the initial energy growth. A magnitude of the numerical abscissa indicates the extent of initial energy growth. The lower bound for the maximum energy growth can be obtained from the Kreiss constant. Finally, the growth function portrays the maximum energy at each timestep optimized over all initial conditions. A more comprehensive and mathematical definitions of the mentioned metrics are given later in Chapter 3.

Figure 2.8b shows the spectral portrait of Poiseullie flow with $Re = 1000$ and $\alpha = 1$ and the lower half of the complex plane is the stable half plane. Under the traditional linear modal stability analysis, the flow is stable since all the eigenvalues (the blue dots) are in the stable half plane. The pseudospectra are shown by the blue contour lines corresponding to perturbations of the order $10^{0.25}, 10^{0.5}, 10^{1}, 10^{2}, 10^{4}$ and it can be seen that perturbations of some orders extend into the unstable half plane. This means that if a perturbation of

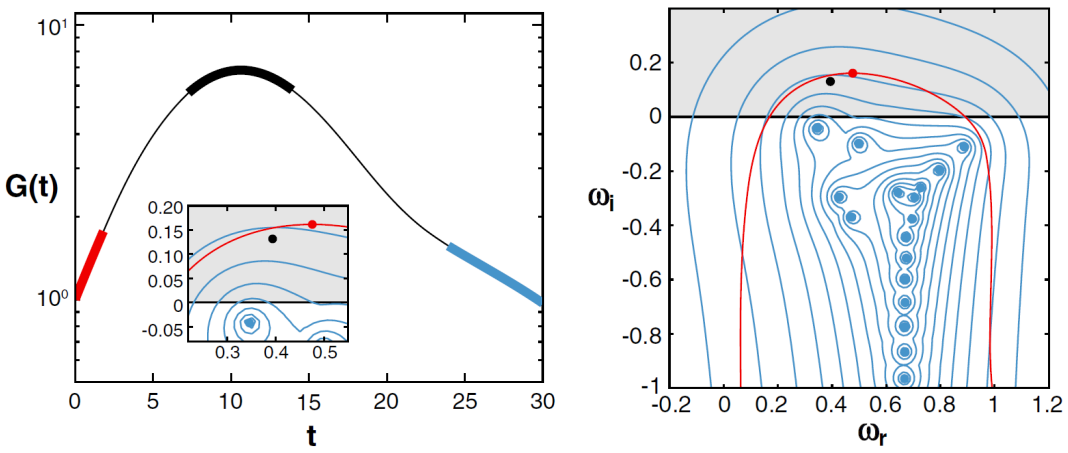

(a) growth rate

(b) spectral portrait

Figure 2.8: Nonmodal stability analysis of Poiseullie flow showing (a) the transient evolution of perturbation energy and (b) the spectra and pseudospectra (Schmid, 2007)

that order is added to the system, the eigenvalues can vary within the corresponding pseudospectral contours, making the system unstable. The red line is the numerical range, the extremity of which in the unstable half plane marks the numerical abscissa. The numerical abscissa is seen significantly protruding into the unstable half plane and therefore an initial energy growth can be expected. The lower energy bound can be calculated from the the Kreiss constant shown as a black dot in figure 2.8b. Figure 2.8a is the growth function in time colour coded to display its relation to the numerical abscissa, Kreiss constant and the fastest growing mode (largest eigenvalue). It is clearly seen that this marginally stable case in terms of modal stability actually exhibits transient energy growth and thus is unstable in finite-time.

Figure 2.9 shows the stability of Poiseuille flow generalized in the $Re-\alpha$ plane. The blue line is the boundary of the unstable region as predicted by linear modal stability analysis. In other words, the region in which the growth rate of the fastest growing mode is positive. It can be seen that the minimum Re value in this region coincides with the famous 5772 value obtained by Orszag (1971). The red line, on the other hand, bounds the unstable region by nonmodal stability analysis, which means that in this region, the numerical abscissa is

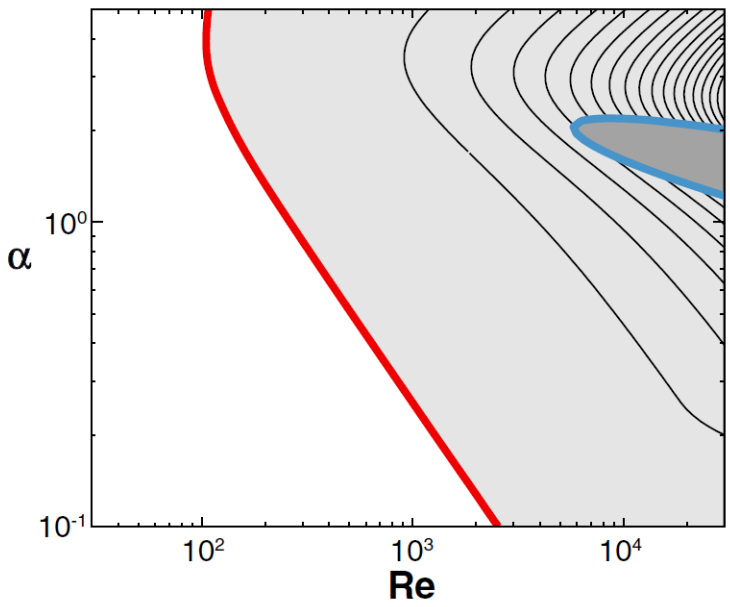

Figure 2.9: Asymptotic and finite time stability regions in the Re-α space for Poiseullie flow (Schmid, 2007)

positive. This gives the minimum unstable Reynold's number to be around 100. Interestingly, the experimental values ranging from 1000–3000 given by Patel and Head (1969) is close to $\alpha = 0.1$ in figure 2.9.

2.6 Summary

Shallow flows, represented as three main cases of shallow jets, wakes and mixing layers, have been prominently studied in literature using experimental, numerical methods as well as stability analysis. Although the linear modal stability approach has been somewhat reasonably used so far, it has been reported in literature since the 1970s that linear stability does not accurately give the conditions for instability for shear flows for the problem of transition to turbulence. Traditional stability theory attributes this discrepancy to the linearization but it is shown that nonnormality of the matrix operator widely found in many shear flows can cause the energy to grow before eventually decaying. Thus, the linear modal stability only gives the limited picture of asymptotic stability. Nonmodal stability is a fairly recent devel-

opment in the hydrodynamic stability field which goes beyond evaluating only the fastest growing mode and shifts the focus on growth energy contained in the initial condition. By using the Poiseuille flow as an example, various publications were used to demonstrate and justify the use of nonmodal stability analysis. In case of shallow flows, there is no literature available to evaluate the transient dynamics of perturbations. With shallow jets, wakes and mixing layers being highly likely to have nonnormal linear operators, it is definitely a problem worth exploring.

Chapter 3

Formulation of Stability Problem

3.1 Governing Equations

The equations of choice used to describe the dynamics of shallow flows are the Saint-Venant equations or shallow water equations. The particular formulation used in this study is derived by depth and time averaging of the full Navier-Stokes equations (Chu et al., 1991; Socolofsky and Jirka, 2004). The validity of rigid lid assumption is thoroughly studied by Ghidaoui and Kolyshkin (1999) and for the purpose of this study, it is sufficient and thus is applied.

$$\frac{\partial \tilde{u}h}{\partial x} + \frac{\partial \tilde{v}h}{\partial y} = 0 \tag{3.1}$$

$$\frac{\partial \tilde{u}}{\partial t} + \tilde{u}\frac{\partial \tilde{u}}{\partial x} + \tilde{v}\frac{\partial \tilde{u}}{\partial y} = -\frac{\partial \tilde{p}}{\partial x} - \frac{c_f}{h}\tilde{u}\sqrt{\tilde{u}^2 + \tilde{v}^2} \tag{3.2}$$

$$\frac{\partial \tilde{v}}{\partial t} + \tilde{u}\frac{\partial \tilde{v}}{\partial x} + \tilde{v}\frac{\partial \tilde{v}}{\partial y} = -\frac{\partial \tilde{p}}{\partial y} - \frac{c_f}{h}\tilde{v}\sqrt{\tilde{u}^2 + \tilde{v}^2} \tag{3.3}$$

The system of equations comprising of (3.1), (3.2) and (3.3) mathematical description of the Saint-Venant Equations with (3.1) being the continuity equation and (3.2) and (3.3) being the momentum equations in the x and y directions respectively. The velocity in the x

direction is denoted by $\tilde{u}$ and that in the y direction by $\tilde{v}$. h is depth of the flow and p is the pressure. Bed friction is quantified by the friction coefficient, c_f, which can either be based on the Chézy bed resistance coefficient or the Manning roughness coefficient (Ghidaoui and Kolyshkin, 1999). Following the stability analyses done by Chu et al. (1991) and (Chen and Jirka, 1997), the Chézy bed resistance coefficient is used.

3.2 Linear Stability Formulation

The general procedure for conducting a linear stability analysis includes the linearization of the governing equations around the base flow. The base flow, in this study, is a parallel unidirectional flow whose transverse velocity profile is given by U. The flow variables are then decomposed into the base flow and the perturbations as follows:

$$\tilde{u} = U(y) + u'(x, y, z) \tag{3.4}$$

$$\tilde{v} = v'(x, y, z) \tag{3.5}$$

$$\tilde{p} = P(x) + p'(x, y, z) \tag{3.6}$$

The prime variables u', $v'$and p' are the added very small perturbations. The base flow is a parallel unidirectional flow and so the y component of the velocity consists only of the perturbation as seen in (3.5). The equations (3.4), (3.5) and (3.6) are then substituted into (3.1),(3.2) and (3.3). Since the perturbation terms are very small, the second order terms are considered negligible, resulting in the perturbation equations given below.

$$\frac{\partial u'h}{\partial x} + \frac{\partial v'h}{\partial y} = 0 \tag{3.7}$$

$$\frac{\partial u'}{\partial t} + U\frac{\partial u'}{\partial x} + v'\frac{\partial U}{\partial y} = -\frac{\partial p'}{\partial x} - \frac{c_f U}{h}u' \tag{3.8}$$

$$\frac{\partial v'}{\partial t} + U\frac{\partial v'}{\partial x} = -\frac{\partial p'}{\partial y} - \frac{c_f U}{2h}v' \tag{3.9}$$

The equations (3.7), (3.8) and (3.9) are then manipulated further to eliminate the pressure term. The derivative of (3.8) with respect to y and that of (3.9) with respect to x are taken. After taking the difference of the resulting two equations, the continuity equation was used to simplify the equation to only one dependent variable, v. The derivation procedure followed is described in (Dewals et al., 2008) where a modified form of the Orr-Sommerfeld equation is derived. However, in this study, only inviscid stability was considered and so the final equation obtained is the Rayleigh equation with the effect of bed friction as opposed to the Orr-Sommerfeld equation. Consequently, a time dependent ordinary differential equation (3.10) is obtained. The prime notation is dropped for simplicity.

$$\frac{\partial v}{\partial t} = f\left(\frac{\partial v}{\partial x}, \frac{\partial v}{\partial y}, U, c_f, h\right) \tag{3.10}$$

According to Fourier analysis, functions can be represented or approximated by waves or a combination of waves. Fourier transform is a common tool in engineering and science for obtaining the dominant waves that make up a function. Using this concept, the perturbations are assumed to be Fourier waves.

$$\phi' = \bar{\phi}(y)e^{ik(x-ct)} \tag{3.11}$$

Equation (3.11) is called a normal mode solution where ϕ represents u,v, or p . The bar notation represents the amplitude of the wave, dependent on y in this case. The parameters k and ω are the wavenumber and frequency of the perturbation, which is important in determining the stability of the system. Further discussion on stability is done later in section 3.6 and the dependence of k and c on the spatial and temporal stability of the system is further elaborated.

$$ikv_{yy}c - ikUv_{yy} + ikvU_{yy} - ik^3vc + ik^3Uv - U\frac{(c_f)_y v_y}{h} - \frac{c_f U_y v_y}{h} - \frac{c_f U v_{yy}}{h} + \frac{c_f U k^2 v}{2h} = 0 \quad (3.12)$$

Equation (3.12) is called a Rayleigh equation for inviscid instability and the subscript notation is adopted for derivatives. It is a so-called Strum-Louisville type differential equation with c being its eigenvalue.

3.3 Velocity Profiles Representing Shallow Flows

The base flow velocity profiles U used in equation 3.12 represent the three shallow flow cases discussed in Chapter 2. The ambient velocity parameter denoted by U_a in equations. The first and second derivations are calculated analytically from the representing functions. The velocity profiles are presented in figures 3.1, 3.2 and 3.3, where the *y-axis* represents velocity and the *x-axis* represents the transverse distance.

The mixing layer profile takes the form, as discussed in Chapter 2 has two different plateaus of velocity with a smooth transitional zone (figure 3.1). This profile is approximated by a hyperbolic tangent function as following Chu et al. (1991); Ghidaoui and Kolyshkin (1999).

$$U(y) = U_a + \frac{1}{2}(1 + tanh(y)) \quad (3.13)$$

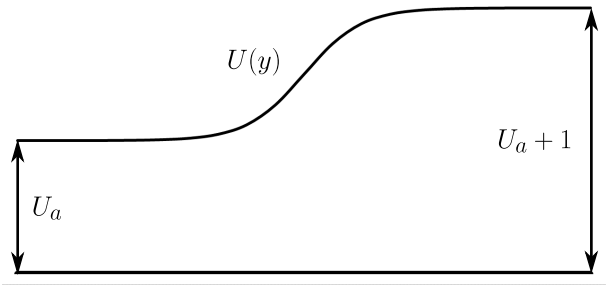

Figure 3.1: Mixing layer velocity profile

The jet case is represented by a Gaussian profile and it is approximated using the hyperbolic secant function as shown in equation 3.14 . The use of the hyperbolic secant function is commonly used to represent the jet profile in literature Chu et al. (1991); Ghidaoui and Kolyshkin (1999).

$$U(y) = U_a + sech^2(y) \tag{3.14}$$

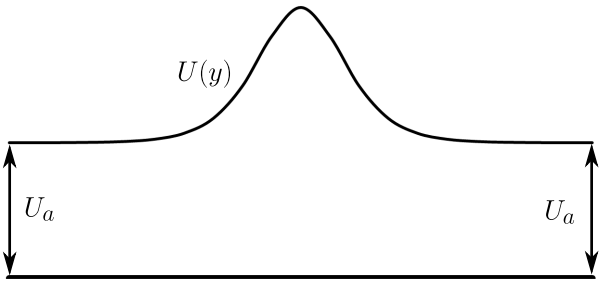

Figure 3.2: Jet velocity profile

The wake profile is also represented by a hyperbolic secant function like the jet profile but with a negative sign, which mirrors the profile about its base.

$$U(y) = U_a - sech^2(y) \tag{3.15}$$

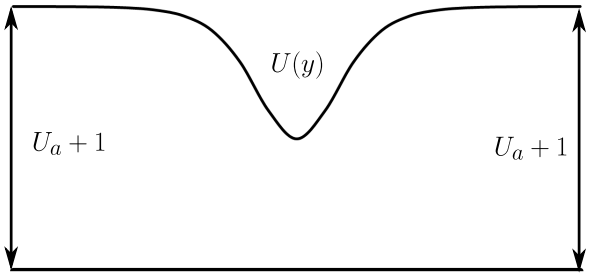

Figure 3.3: Wake velocity profile

3.4 Bed Friction

From the literature on the onset, growth and dynamics of large-scale turbulent coherent structures in shallow flows, it is shown that the bed friction plays a vital role in the flow dynamics. Wolanski et al. (1984) developed a dimensional parameter which is essentially a ratio of the generation of vorticity to the cancellation of vorticity. Another study by Chu et al. (1983) introduced the bottom friction stability parameter S, as given by equation (3.16). Similar to the concept in Wolanski et al. (1984), S is derived from the ratio of the rate of dissipation of energy form the larger-scale eddies by bottom friction to the rate of energy input into these eddies by the mean shear. The parameter S, which will be referred to as the bed friction number is commonly used in many studies of shallow flows.

$$S = \frac{c_f}{2h}\frac{U}{U_y} \tag{3.16}$$

In particular, the parameter of interest is actually the bed friction number at the inflection point of the velocity profile, denoted by $\overline{S}$.

3.5 Solution to the Linear Stability Problem

The differential equation (3.12) is numerically solved using the Chebyshev spectral method. Unlike finite difference methods which use the neighbouring nodes to approximate the deriva-

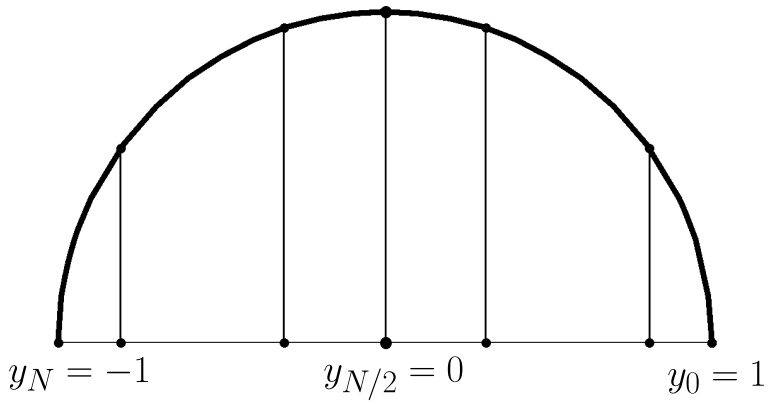

Figure 3.4: Chebyshev points

tive at certain locations, spectral methods use the entire domain by approximating the solution with polynomials. The computational domain is discretized into nodes using Chebyshev points, which are equidistant points on a circumference of a circle projected onto a line. Mathematically, the Chebyshev points are given as below.

$$y_j = \cos(j\pi/N), \quad j = 0, 1, ..., N \tag{3.17}$$

Chebyshev points are ideal for polynomial interpolation. Lagrangian polynomials are used to approximate the solution. This procedure enables the calculation of the derivative terms using Chebyshev differentiation matrices , $\mathbf{D}$. A detailed explanation of this mathematical procedure can be found in Trefethen (2000) and the Chebyshev differentiation matrix is given by:

$$
D_N = \begin{array}{|c|c|c|}
\hline
\frac{2N^2+1}{6} & 2\frac{(-1)^j}{1-x_j} & \frac{1}{2}(-1)^N \\
\hline
-\frac{1}{2}\frac{(-1)^i}{1-x_i} & \frac{(-1)^{i+j}}{x_i-x_j} \quad \frac{-x_j}{2(1-x_j^2)} \quad \frac{(-1)^{i+j}}{x_i-x_j} & \frac{1}{2}\frac{(-1)^{N+i}}{1+x_i} \\
\hline
-\frac{1}{2}(-1)^N & -2\frac{(-1)^{N+j}}{1+x_j} & -\frac{2N^2+1}{6} \\
\hline
\end{array}
\tag{3.18}
$$

The differential operators are than replaced by the Chebyshev differential equations as follows:

$$\mathbf{D} = \frac{\partial}{\partial y} \tag{3.19}$$

$$\mathbf{D}^2 = \frac{\partial^2}{\partial y^2} \tag{3.20}$$

The relationships (3.19) and (3.20) are then substituted into (3.12) which results in a purely algebraic equation over the domain of $[-5, 5]$ in the y direction. After rearranging, the equation can be written as a generalized eigenvalue problem with ω as the eigenvalue problem.

$$\mathbf{A}\hat{\mathbf{v}} = c\mathbf{B}\hat{\mathbf{v}} \tag{3.21}$$

where

$$\mathbf{A} = iUkD^2 - ikU_y y - iU(y)k^3 + \frac{(c_f)_y U}{h}D + \frac{c_f U_y}{h}D + \frac{c_f U}{h}D^2 - \frac{c_f U k^2}{2h}$$

$$\mathbf{B} = ikD^2 - ik^3$$

The resulting eigenvalue problem is solved in MATLAB using the eig function. The matrix $\mathbf{C} = \mathbf{B^{-1}A}$ is used for the solution instead of the generalized eigenvalue problem itself to be consistent with the nonmodal analysis, as explained further in the following sections.

3.6 Growth Rate of Perturbations

The mathematical derivations necessary for linear modal stability have been established. In the modal approach, the attention is focused on the most unstable mode which is obtained from the largest eigenvalue. The growth of perturbations can occur in both space and time and so the stability analyses can be done in time, space or a combined spatio-temporal stability analysis. The eigenvalues of the temporal stability problem are c, the temporal frequency, while that of the spatial stability problem is k, the wavenumber.

A combined analysis of perturbations in space and time can be done by considering both c and k to be complex variables. The growth rate of the temporal and spatial modes correspond to the imaginary parts of c and k. The growth of perturbations in space and time are either of absolute or convective nature. Absolute stability is the growth of perturbations in all directions from a point in space while convective stability is that which grows and is convected downstream with the flow.

Spatial stability is the analysis of the growth of perturbations in space. This can be done by confining the temporal frequencies to only real values i.e. $c = c_r$ and calculating

complex wavenumbers ($k = k_r + k_i$). The problem is now an eigenvalue problem where the eigenvalues are k rather than c. However, spatial stability problem is much more mathematically challenging as the stability equation is a higher order eigenvalue problem. It has also been pointed out in Huerre and Monkewitz (1990) that purely real temporal frequency is not appropriate and so, many of the existing studies are done in the spatio-temporal sense.

However, the focus of this thesis is the evaluation of transient perturbation energy growth in finite time and so, the stability analysis of interest is temporal. From equation 3.21, the value of the c can be calculated as the eigenvalue of the system. In temporal stability problems, only real wave numbers are considered and the frequency values of complex numbers i.e. $k = k_r$ and $c = c_r + ic_i$. The imaginary part of c is the growth rate of the perturbations in time and the real part is the speed of the wave. A positive perturbation growth rate means that the small perturbations will exponentially grow in time and eventually will be large enough to alter the flow field.

The spectrum is defined as the set of eigenvalues of $\mathbf{C} = \mathbf{B^{-1}A}$. They are conveniently visualized on the complex plane. As mentioned earlier, the imaginary part of the eigenvalues corresponds to the growth rate and thus the upper half of the complex plane is called the unstable half plane. If all the eigenvalues lie within the lower half, the system is stable. If any eigenvalue lies in the unstable half plane, the system is unstable. Therefore, the largest eigenvalue, corresponding to the fastest growing mode, is focused on in linear modal temporal stability analysis.

3.7 Nonmodal Stability Analysis

In order to conduct nonmodal stability analysis, the system will be considered as an initial value problem, rather than an eigenvalue problem. Conveniently, the mathematical procedure does not have to be repeated. Using the same derivations, the system 3.21 can be rewritten as:

$$\frac{\partial \mathbf{v}}{\partial t} = -i\mathbf{C} \tag{3.22}$$

The nonnormality of $\mathbf{C}$ is evaluated and the nonmodal analysis metrics such as the pseudospectra and numerical abscissa are evaluated. The growth function is also used to evaluate the finite time growth of perturbation energy. The definitions and descriptions of these terms are given in the following sections.

3.8 Measure of Nonnormality

As mentioned earlier, the results of linear stability analysis is incomplete for nonnormal matrix operators and so it is important to know if a matrix is normal or nonnormal. Many definitions of a nomormal matirx exist but for our purposes the formal definition of a normal matrix given by (Trefethen and Embree, 2005) in terms of eigenvectors is as follows:

A matrix $\mathbf{A} \in \mathbb{C}^{N\times N}$ is normal if it has a complete set of orthogonal eigenvectors, that is, if it is unitarily diagonalizable:

$$\mathbf{A} = \mathbf{V}\mathbf{\Lambda}\mathbf{V}^T \tag{3.23}$$

The subject of nonnormality is complex but Trefethen and Embree (2005) suggested the use of condition number to get an idea of the nonnormality of the operator.

$$\kappa = \|\mathbf{V}\| \left\|\mathbf{V}^{-1}\right\| = \frac{s_{max}}{s_{min}} \tag{3.24}$$

The condition number of a matrix can be calculated using (3.24) where $\mathbf{V}$ is the matrix whose columns are eigenvectors $\mathbf{v}$ of the matrix of interest. The expression can also be written as the ratio of the maximum singular value to the minimum singular value of $\mathbf{V}$. If $\kappa = 1$, $\mathbf{C}$ is a normal matrix and if $\kappa > 1$, the matrix is nonnormal. In a sense, the magnitude of the condition number reflects the degree of nonnormality, with higher condition numbers suggesting higher degrees of nonnormality.

3.9 Pseudospectra

Pseudosptra are used as a complement to the spectra in nonmodal stability analysis and they are very useful in visualizing nonmodal stability (Trefethen et al., 1993; Schmid, 2007). There exist many definitions of pseudospectra or pseudo-eigenvalues which Trefethen and Embree (2005) covers in detail. However, for simplicity, only one definition is presented in this paper. The pseudospectrum of a matrix $\mathbf{A}$, denoted by $\sigma_\epsilon(\mathbf{A})$, is defined as the set of eigenvalues obtained by perturbing the matrix $\mathbf{A}$ with a matrix $\mathbf{E}$ whose norm is ϵ.

$$\sigma_\epsilon(\mathbf{A}) \text{ is a set of } \lambda \in \mathbf{C} \text{ such that },\lambda \in \sigma(\mathbf{A}+\mathbf{E}) \text{ for some } \mathbf{E} \in \mathbf{C}^{N\times N} \text{ with } \|E\| < \epsilon$$

Pesudospectra can be plotted as contour lines of ϵ superimposed on the spectral plot. Similar to spectral analysis where the position of the largest eigenvalue in the complex plane must remain in the stable region, which is the lower half of the plane in this paper, for the flow to be stable, pseudospectra of the range of perturbation values of interest should also be in the stable region. Pseudospectra are indications of the sensitivity of the system to perturbation. Depending on how much the pseudospectra protrude into the unstable region, the system is nonmodally unstable and instabilities of significant order can exist in finite time before dissipating as $t \to \infty$. The maximum distance that the pseudospectra protrude into the unstable region is called the pseudospectral abscissa and it is related to the bounds of the energy growth (Trefethen and Embree, 2005).

The computation of pseudospectra is conducted using the MATLAB software package EIGTOOLS developed by the Oxford University computing laboratory (Wright, 2000). It uses the ARPACK for solving large scale eigenvalues to compute the pseudospectra.

3.10 Transient Energy Growth

Using nonmodal analysis, the response of the system to the most dangerous initial condition, which amplifies the perturbation energy to the maximum, is evaluated. The growth function

is $G(t)$ given by

$$G(t) = \max_{q_0} \frac{\|q(t)\|}{\|q_0\|} = \max_{q_0} \frac{\left\|e^{-i\mathbf{C}t} q_0\right\|}{\|q_0\|} = \left\|e^{-i\mathbf{C}t}\right\| \tag{3.25}$$

that can be used to analyze the evolution of the energy in the system in a specified time interval optimized over all initial conditions (Schmid, 2007).

The major difference between spectral and nonmodal analyses is that spectral analysis only considers the fastest growing mode, which is equivalent to having a growth function of $g(t) = e^{-itc_i}$, where c_i is the imaginary part of the fastest growing eigenvalue, which does not give any consideration to the eigenfunctions of $\mathbf{C}$ (Schmid, 2007). Systems of equations that result in a nonnormal linear operator greatly amplify the energy contained in the initial condition before dissipation. The transient amplification of energy in the growth function can verify that spectral analysis can only predict the asymptotic fate of the system.

3.11 Summary

The mathematical formulation of the modal and nonmodal stability problem was given in this chapter. The governing equations are the depth-averaged Saint Venant equations or the shallow water equations with the friction coefficient.

The modal stability problem was derived by assuming a base flow and perturbations and linearizing the governing equations about the base flow. A wavelike solution is assumed for the perturbations, which is equivalent to taking a Fourier transform. The resulting system, after some mathematical manipulation, becomes the Rayleigh equation for inviscid stability. The equation is solved by Chebyshev spectral method, which results in an eigenvalue problem.

The nonmodal stability analysis is done by using the same matrix operator from the eigenvalue problem from the modal analysis. The parameters of interest here are the condition number, the numerical abscissa, the pseudospectra and the growth function. These metrics shed light on to the transient dynamics of the perturbations.

Chapter 4

Nonmodal Behaviour of Critical Cases in Modal Analysis

The main objective of this chapter is to revisit the traditional linear modal stability analysis approach and evaluate how the resulting asymptotically stable conditions fit into the bigger picture of transient dynamics. An eigenvalue analysis described in Chapter 3 is conducted and the marginally stable cases in the S-k plane are obtained. Each of these cases have a corresponding linear operator and so the pseudospectral portraits and numerical abscissas, which gives an indication of transient growth, can be obtained. Finally, the transient behaviour of perturbation can be verified with the growth function.

4.1 Growth Rate of the Fastest Growing Modes

When perturbations are introduced to the flow, they will either grow exponentially, hence the instability, or they will decay and have no effect on the flow. In Chapter 3, it was established that linear stability in time is evaluated through the growth rate kc_i of the fastest growing mode, which is obtained from the wavenumber k the imaginary part of the largest eigenvalue c of the system. In this chapter, the growth rate is normalized as $(kc_i)_{max}/U_y$ using the velocity gradient at the inflexion point. Since the main energy dissipation mechanism for

shallow flows is bed friction, the growth rate of the perturbations is evaluated as a function of the bed friction number. Shallow mixing layers, jets and wakes profiles were evaluated for different ambient velocity parameters U_a. For the mixing layer and jet profiles, the U_a values considered were $0.1, 0.3, 0.5, 1, 5, 10$. As for the wake profile, values less than one were not possible to evaluate since this resulted in negative streamwise velocities in the profile. Therefore, the values selected are $1.1, 1.3, 1.5, 1, 5, 10$.

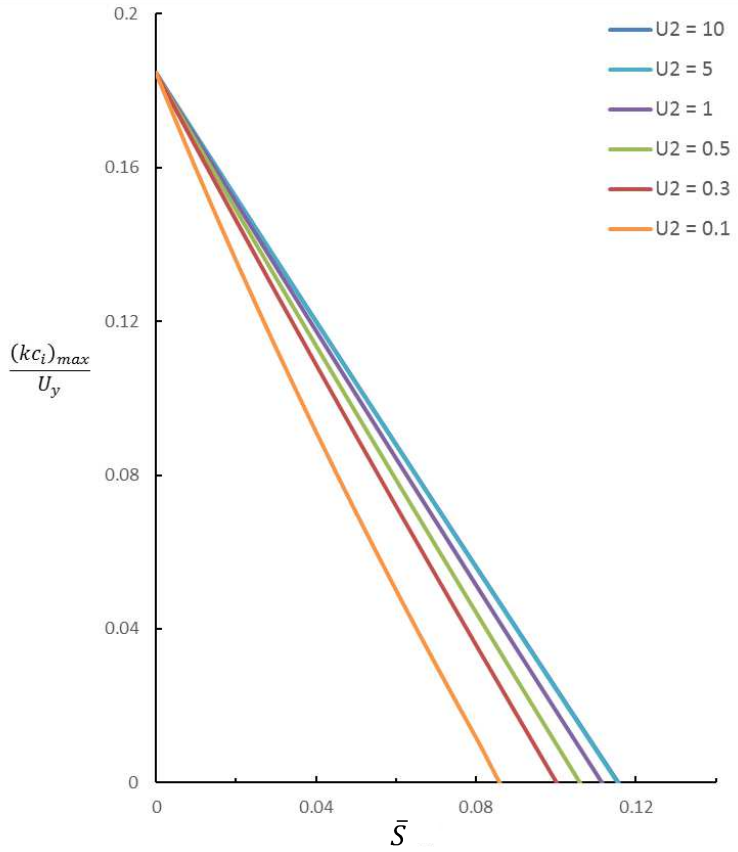

Figure 4.1: Variation of maximum growth rates of the most unstable modes with respect to the bed friction number at inflection for $U_a = 0.1, 0.3, 0.5, 1, 5, 10$ for the mixing layer velocity profile

Figure 4.1 shows the normalized growth rate plotted against the bed friction number at inflexion point for the mixing layer profile. The linear dependence of the normalized growth rate on the inflexion bed friction number is in agreement with Chu et al. (1991). The lower the ambient velocity parameter, the steeper the slope of the line, which means

that the rate of energy dissipation as bed friction number increases is higher. As ambient velocities increase, the slope of the line also becomes less steep and the intersection with the y-axis is also shifted further, suggesting that the flow becomes more unstable and higher bed friction is required to stabilize the flow. For the two ambient velocity values of $U_a = 5, 10$, the lines are almost identical. This is due to the fact that at a certain ambient velocity, there is a convergence for the bed friction required to stabilize the flow. The critical bed friction numbers at the inflexion points for the mixing layer profile correspding to $U_a = 0.1, 0.3, 0.5, 1, 5, 10$ are $\overline{S}_{crit} = 0.087, 0.101, 0.106, 0.112, 0.116, 0.116$. The wavenumbers are $k_{crit} = 0.53, 0.51, 0.5, 0.49, 0.49, 0.49$. It can be seen that the wavenumbers for the cirtical cases decreases with the increase of ambient velocity. Thus, the wavelength of the most amplified mode increases with ambient velocity.

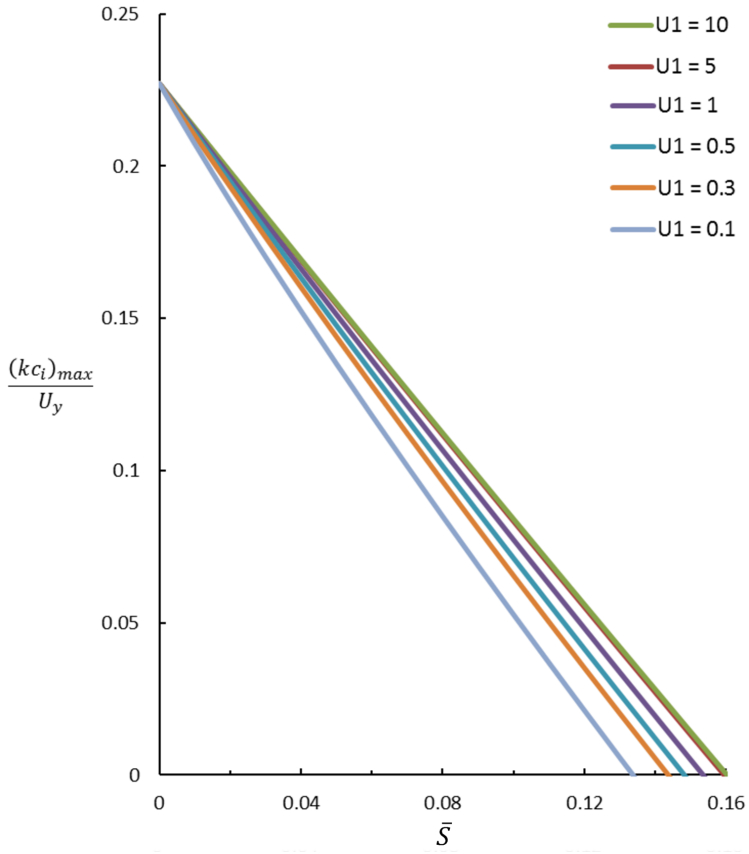

Figure 4.2: Variation of maximum growth rates of the most unstable modes with respect to the bed friction number at inflection for $U_2 = 0.1, 0.3, 0.5, 1, 5, 10$ for jet velocity profile

A similar plot to figure 4.1 for the jet velocity profile is shown in figure 4.2. Linearly decreasing growth rates as a function of the inflection bed friction number are also observed. This is also in agreement with results reported in Chu et al. (1991). Although the trend of steeper slopes with lower ambient velocity parameters holds, the increase in the slope of the lines is not as much as the mixing layer case. The jet velocity profiles have higher critical bed friction numbers compared to the mixing layer. The highest critical bed friction in the mixing layer case does not exceed 0.12, while in the jet case, even the critical bed friction for $U_a = 0.1$ is higher than 0.12, suggesting that the jet profile is much more unstable than the mixing layer profile. The convergence of critical bed friction with the increase of the ambient velocity parameter is also observed in this case. The critical bed friction numbers inflection points for the jet profile correspond to $U_a = 0.1, 0.3, 0.5, 1, 5, 10$ are $\overline{S}_{crit} = 0.136, 0.144, 0.149, 0.154, 0.16, 0.161$. The wavenumbers are $k_{crit} = 1.23, 1.13, 1.08, 1.03, 0.97, 0.96$. The critical wavenumbers for this case are also decreasing with the increase of ambient velocity, suggesting that larger waves (higher wavelengths) are amplified with higher ambient velocities. However, the critical wavelengths for the jet profile are approximately twice larger than that of the mixing layer profile. Hence, the modes amplified in the jet profile are much smaller than that of the mixing layer.

The last case of interest is the wake profile and its corresponding plot for the growth rate versus bed friction is given in figure 4.3. Similar to the previous two cases, the dependence of growth rate on bed friction is linear. Lower ambient velocity parameters have steeper slopes, as observed in other cases as well. However, the decrease seems to be more for lower ambient velocities as seen in the drastic decrease in the critical bed friction number from $U_a = 1.3$ to $U_a = 1.1$. The convergence of bed friction for higher ambient velocity parameters also holds in this cases. The main characteristic of this case that stands out is the wider range of critical bed friction numbers. The bed friction numbers at the two highest ambient velocity parameters $U_a = 5, 10$ are around 0.16, which is comparable to the jet profile. On the other hand, that of the lower end is closer to 0.08, which is much lower than what is seen in the jet profile (0.136). The lower ambient velocity are more comparable to the mixing layer case,

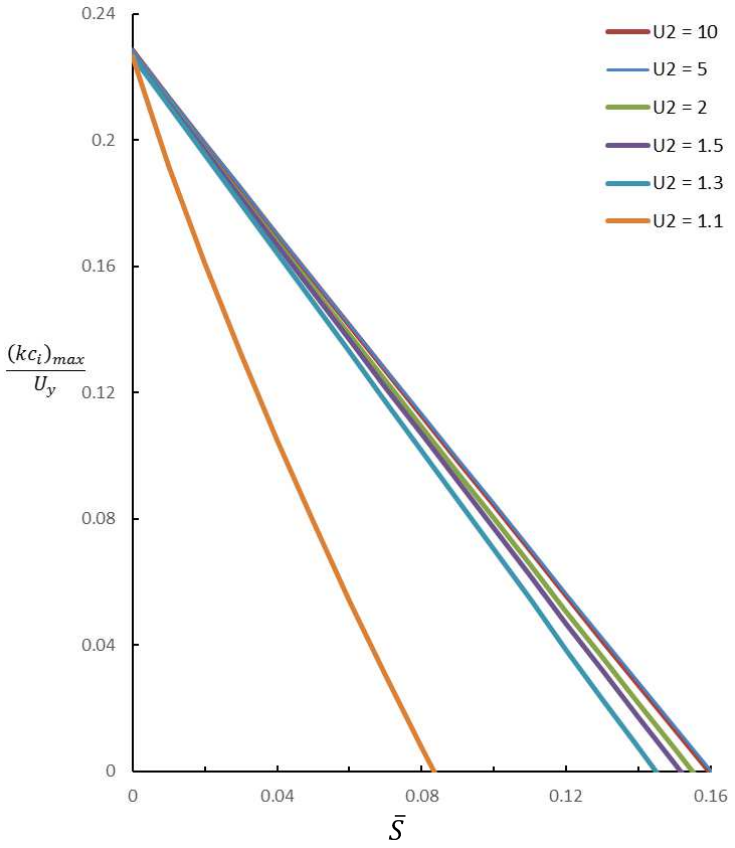

Figure 4.3: Variation of maximum growth rates of the most unstable modes with respect to the bed friction number at inflection for $U_2 = 0.1, 0.3, 0.5, 1, 5, 10$ for the wake velocity profile

although the ambient parameters on the lower end are different. The critical bed friction numbers at the inflexion points for the wake profile correspond to $U_a = 1.1, 1.3, 1.5, 2, 5, 10$ are $\overline{S}_{crit} = 0.136, 0.144, 0.149, 0.154, 0.16, 0.161$. Note that the values of U_a chosen to for the wake profile are different than those chosen for the mixing layer and jet profile in order to keep the profile positive. The wavenumbers are $k_{crit} = 1.1, 0.85, 0.9, 0.9, 0.9, 0.95$. The wavenumbers decreased with the increase of ambient velocity but in this case, there is also an anomaly. The wavenumber corresponding to $U_a = 1.1$ is $k_crit = 1.1$, which is higher than that for $U_a = 1.3$ which is $U_a = 0.85$. This anomaly is most likely to be a numerical error since the matrix comes closer to becoming a singular matrix as the ambient velocity parameter decreases.

Table 4.1: Critical values of bed friction number and the corresponding wavenumber for the mixing layer velocity profile

		$U_a = 0.1$	$U_a = 0.3$	$U_a = 0.5$	$U_a = 1$	$U_a = 5$	$U_a = 10$
Mixing layer	Bed friction number	0.087	0.101	0.106	0.112	0.116	0.116
	Wavenumber	0.53	0.51	0.5	0.49	0.49	0.49
		$U_a = 0.1$	$U_a = 0.3$	$U_a = 0.5$	$U_a = 1$	$U_a = 5$	$U_a = 10$
Jet	Bed friction number	0.136	0.144	0.149	0.154	0.16	0.161
	Wavenumber	1.23	1.13	1.08	1.03	0.97	0.96
		$U_a = 1.1$	$U_a = 1.3$	$U_a = 1.5$	$U_a = 2$	$U_a = 5$	$U_a = 10$
Wake	Bed friction number	0.083	0.145	0.152	0.155	0.16	0.16
	Wavenumber	1.1	0.85	0.9	0.9	0.9	0.95

The analysis of figures 4.1,4.2 and 4.3 presented above is summarized in table 4.1. These critical values of $\overline{S}$ and k are ordered pairs representing a coordinate in the S-k space. Each pair has a linear operator, which is used for further analysis in the nonmodal approach.

4.2 Modal Stability Regions

In section 4.1, the critical bed friction numbers are identified in terms of the maximum growth rate over all wavenumbers. The current section generalizes the results the linear modal stability analysis on the S-k plane in the form of unstable regions, within which the growth rate of the perturbations is positive. Only the higher four values of ambient velocity presented in the last section are further analysed here.

Figures 4.4a-d shows the unstable regions for the mixing layer profile corresponding to the ambient velocity values $0.5, 1, 5$, and 10 respectively. The unstable regions are parabolic in shape and increase in size with increasing ambient velocity values. This is consistent with the observations from the previous section and suggests that the higher the ambient

velocity, the more unstable the flow becomes and therefore a higher bed friction is required to stabilize the flow. At lower bed friction numbers, the range of unstable wavenumbers is wider and as the bed friction number increases, the range of unstable wavenumbers become narrower. Thus, more and more wave components of the perturbations get dissipated with higher bed friction numbers. The critical bed friction and wavenumber values presented in the last section correspond to the point (S, k) at the peak of the parabolas.

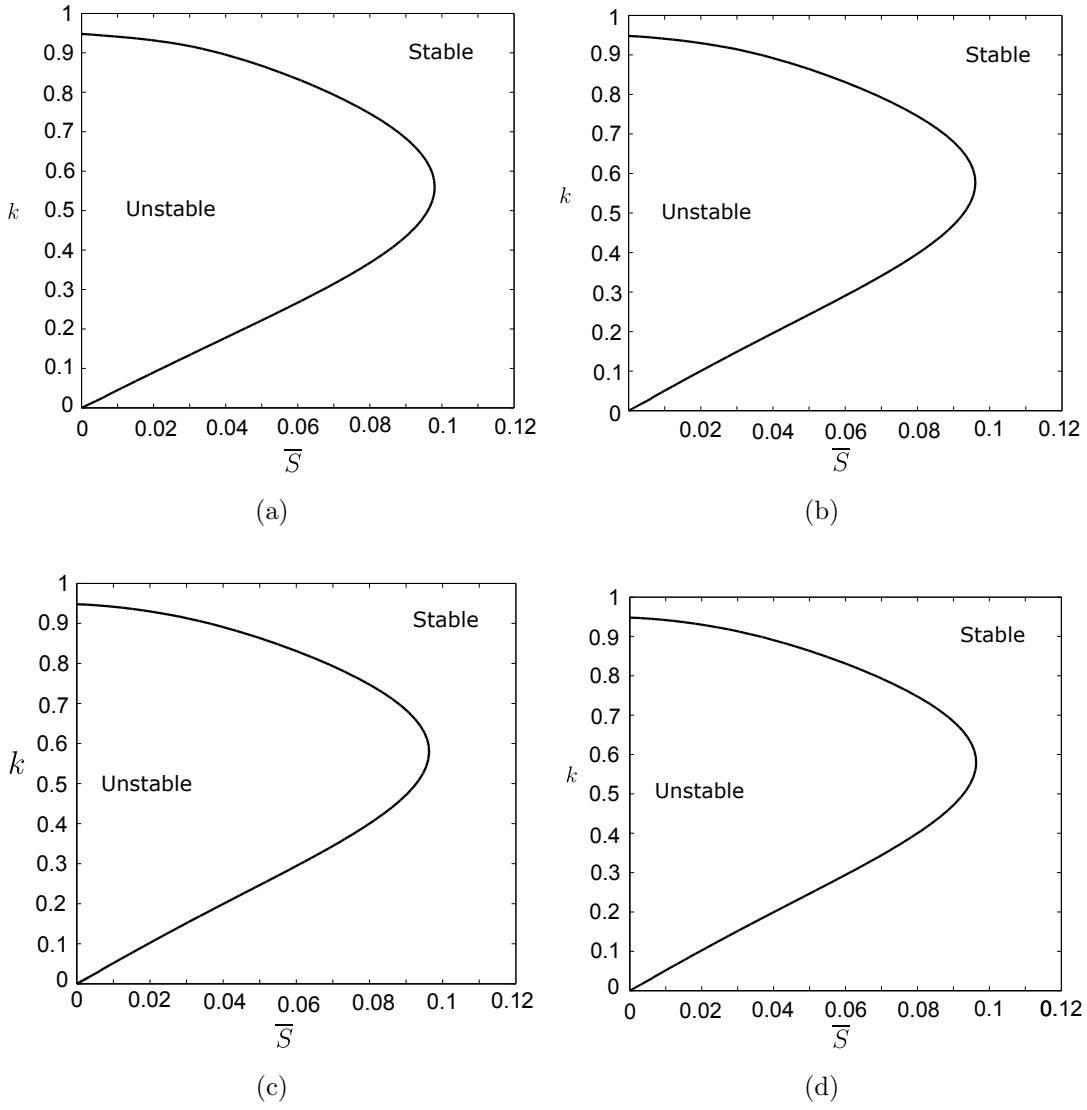

Figure 4.4: Unstable regions in the S-k space obtained from linear modal stability analysis for the mixing layer profile with (a)$U_a = 0.5$, (b)$U_a = 1$, (c)$U_a = 5$, (d) $U_a = 10$

Similar unstable regions are also observed in the case of the jet profile and are shown in figures 4.5a-d or the ambient velocities of $0.5, 1, 5$, and 10. The unstable regions grow as the ambient velocity increases and the peak of the parabolas are the critical cases reported in the previous section. The regions are parabolic but are skewed toward the higher wavenumbers. The range of wavenumers for the no-friction case is about twice larger than the mixing layer case. This is reasonable since the critical wave numbers are also twice larger and these valuse are found at approximately half of the wavelength range, which is where the peak of the parabolas are.

Lastly, the unstable regions of the wake profile with ambient velocities $1.5, 2, 5$, and 10 are given in figures 4.6a-d. Similar to the previous two cases, the unstable regions are of a parabola-like shape. In these cases, the peak is more or less in the center with respect to the base. The unstable region increases with ambient velocity. The range of wavenumbers for the no-friction case is comparable to the jet profile. These regions are also in agreement with the results from the previous section and Chu et al. (1991).

4.3 Nonnormality of the Critical Cases

As defined in Chapter 2, normal matrix has eigenvectors which are orthogonal to one another. The deviation from normality or nonnormality of a linear operator is the reason modal stability does not give a full picture of stability Trefethen et al. (1993); Trefethen and Embree (2005), to evaluate if the results of the modal stability given in sections 4.1 and 4.2, the condition number, the choice of measure for nonnormality of a matrix adopted in this theis (see Chapter 3 is computed for some of the critical cases).

Table 4.2 summarizes the condition numbers for the critical cases of modal stability analysis for different ambient velocity parameters. The condition number is equal to unity for normal matrices and the higher the condition number, the more deviated from normality the matrix is. It can be seen that all values are greater than one although a decrease of condition number is seen with an increase in ambient velocity parameter. Some condition

Table 4.2: Measure of nonnormality by the condition number for the mixing layer, jet and wake profiles

	$U_a = 0.5$	$U_a = 1$	$U_a = 5$	$U_a = 10$
Mixing layer	730.76	186.27	6.56	2.73
	$U_a = 0.5$	$U_a = 1$	$U_a = 5$	$U_a = 10$
Jet	294.47	73.57	3.94	2.03
	$U_a = 1.5$	$U_a = 2$	$U_a = 5$	$U_a = 10$
Wake	12.34	9.55	3.58	1.92

numbers are very high with values exceeding 500 indicating that the matrix can be highly nonnormal.

Therefore, the modal analysis results are not cases of no energy growth, but rather asymptotic energy growth. Initial amplification of energy is expected in all cases and further evaluation by means of nonmodal stability analysis is warranted.

4.4 Spectral and Pseudospectral Portrait

The growth rate of the fastest growing mode and the conditions in the S-k space for stability is presented in the previous section. Further analysis is conducted using the nonmodal approach, which instead of focusing the attention on the fastest growing mode, looks closely at all the eigenvalues and their interaction. The same three cases of shallow flows (i.e. mixing layers, jets and wakes) are analysed for the highest three ambient velocity parameters given in sections 4.1 and 4.2. The spectrum, the set of all the eigenvalues, and the pseudospectrum, for which many definitions exist, are evaluated. The pseudospectra are evaluated for perturbations of the order $\epsilon = 10^{-1}, 10^{-2}, 10^{-3}$ and are displayed in the log scale. The plots are on the complex plane and correspond to c_r and c_i respectively. The axis labels are omitted as it is commonly done so in literature. The spectral and pseudospectral portraits of the linear

operator $\mathbf{C}$ are plotted using EigTool by Oxford University Computing Laboratory Wright (2000).

The horizontal line across the figures 4.7, 4.8 and 4.9 separates the stable and unstable half-planes, located on the bottom and top of the line respectively. The dashed circular line represent the numerical range. The furthest point on the numerical range, extending into the unstable half-plane is called the numerical abscissa. The numerical abscissa is directly proportional to the slope of the initial perturbation energy growth and thus an indicator of finite time instability. The black dots represent the spectra and since all the cases presented here are asymptotically stable cases obtained from linear modal stability analysis, they are all in the stable half-plane. The contour lines around the spectra are the pseudospectra of different perturbations.

Table 4.3: Pseudospectral abscissa values for mixing layer profile

	$U_2 = 1$	$U_2 = 5$	$U_2 = 10$
$\epsilon = 10^{-1}$	1.195	1.06	1.035
$\epsilon = 10^{-2}$	0.15	0.16	0.16
$\epsilon = 10^{-3}$	0.013	0.008	0.008

Figure 4.7 shows the spectral and pseudospectral portraits for the mixing layer profile. The asymptotic stability of these cases are confirmed by the location of the spectrum in the stable half-plane. The shape of the spectrum is a slightly tilted H-shape with a few eigenvalues around the shape. The highest eigenvalue is located on the stability margin directly above the H-shape. As ambient velocity increases, the H-shape becomes more horizontal with the location of the highest growing mode remaining more or less in the same position. On the other hand, the numerical abscissa extends considerably into the unstable half-plane, making the spectra and pseudospectra appear small in comparison. The right sides of figure 4.7 show a close up of the spectra and pseudospectras for $\epsilon = 10^{-1}, 10^{-2}, 10^{-3}$. The pseudospectras for figures (4.7a-c) all extend into the unstable plane with the system being most

sensitive to perturbations of the order $\epsilon = 10^{-1}$, for which the pseudospetra encloses the entire spectrum. Similarly, the magnitude of protrusion into the unstable region is quantified as pseudospectral abscissa as seen in Table 4.3. The pseudospectral abscissa is seen to be decreasing 65% for $\epsilon = 10^{-1}$,67% for $\epsilon = 10^{-2}$ and 95% for $\epsilon = 10^{-2}$.

Table 4.4: Pseudospectral abscissa values for jet profile with constant depth

	$U_2 = 1$	$U_2 = 5$	$U_2 = 10$
$\epsilon = 10^{-1}$	1.245	1.165	1.158
$\epsilon = 10^{-2}$	0.192	0.206	0.207
$\epsilon = 10^{-3}$	0.007	0.006	0.005

The spectral and pseudospectral portraits for the jet profile are given in figure 4.8. The situation of the spectra in the stable half-plane aligns with the selected cases being asymtotically stable. The main branch of the spectrum is T-shaped with some outlying eigenvalues, one of which is the fastest growing mode, located on the stability margin. The numerical range for the jet profile is also a circular region similar to that of the mixing layer profile. However, the size of the numerical range is much smaller with the radius about half compared to the mixing layer cases of corresponding ambient velocities. Nevertheless, the numerical range still protrudes into the unstable half-plane, which is indicative of initial perturbation growth. The pseudospectra for $\epsilon = 10^{-1}$ is largely circular with the smaller bump on the right side. The pseudospectra are also seen to be protruding into the unstable half-plane. The values of the pseudospectral abscissa for $\epsilon = 10^{-1}, 10^{-2}, 10^{-3}$ are given in table 4.4. The decrease in pseudospectra is observed as ambient velocity values.

The spectra and pseudospectra are also calculated for the wake profile given in figure 4.9. Unlike the mixing layer and jet profiles, the shape of the spectra does completely shift as seen from figure 4.9a to 4.9b. The shape of the spectrum is a horizontal T-like shape pointing to the left with some outliers, one of which is the fastest growing mode. The longer arm is bent down at $U_a = 1.5$ and becomes more horizontal as the ambient velocity

Table 4.5: Pseudospectral abscissa values for wake profile with constant depth

	$U_a = 2$	$U_a = 5$	$U_a = 10$
$\epsilon = 10^{-1}$	0.575	0.617	0.606
$\epsilon = 10^{-2}$	0.065	0.051	0.048
$\epsilon = 10^{-3}$	-0.004	-0.0134	-0.01

increases. The shape of the numerical range is circular and partially in the unstable half-plane, consistent with both the mixing layer and jet profiles but the size does not change much with ambient velocity change. Initial energy growth is thus expected. The shape of the pseudospectra is consistent with the shape of the spectrum. The pseudospectra resembles that of jet profile but mirrored around the vertical axis. Some portions of the pseudospectra are still crossing over to the unstable half-plane in plane, which suggests transient growth for some perturbations. The pseudospectral abscissa values are reported in table 4.5.

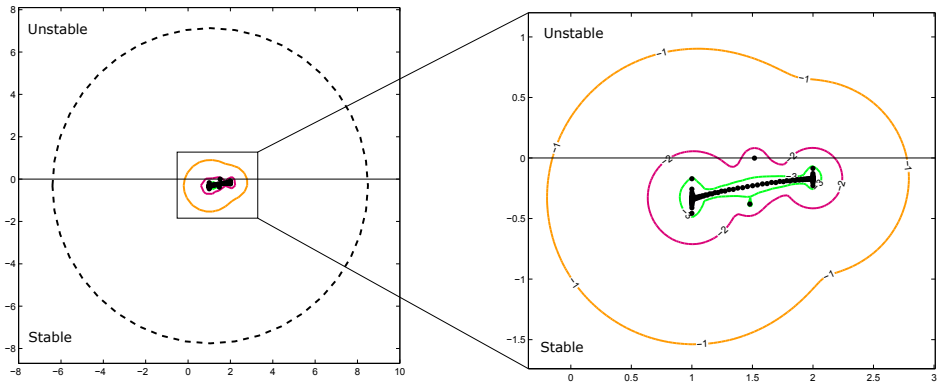

(a)

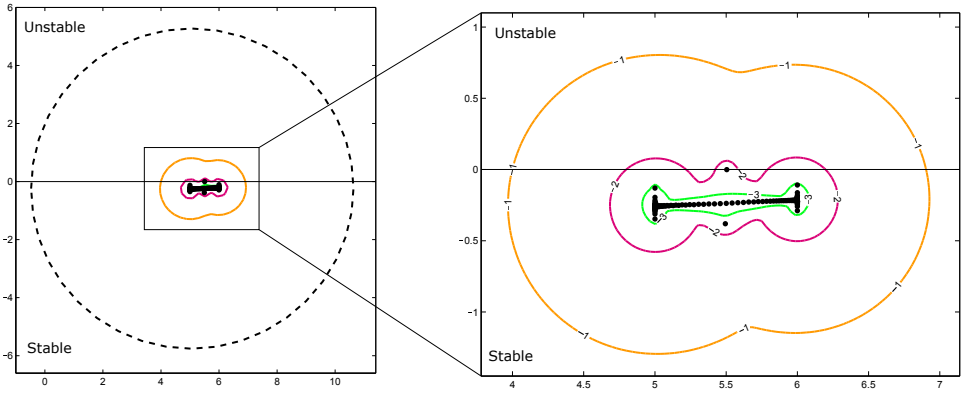

(b)

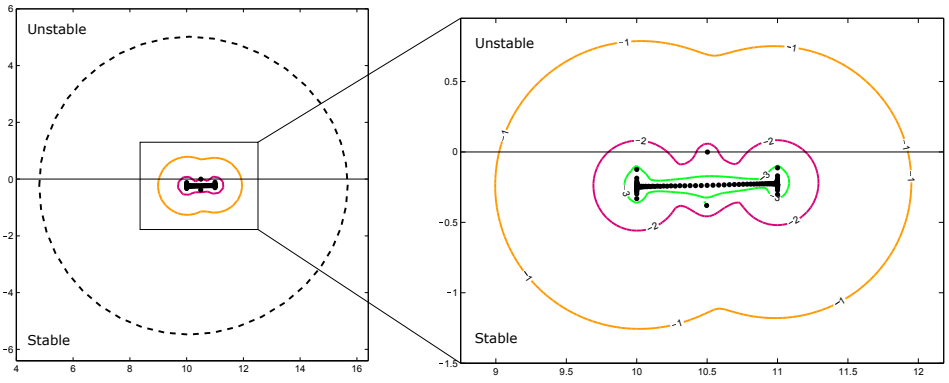

(c)

Figure 4.7: Spectral portraits of asymptotically stable cases for the mixing layer velocity profile and (a) $U_2 = 1$, (b) $U_2 = 5$, (c) $U_2 = 10$

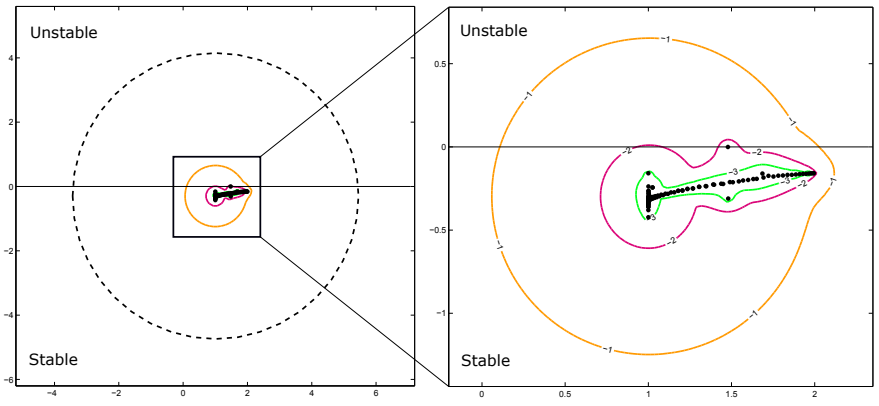

(a)

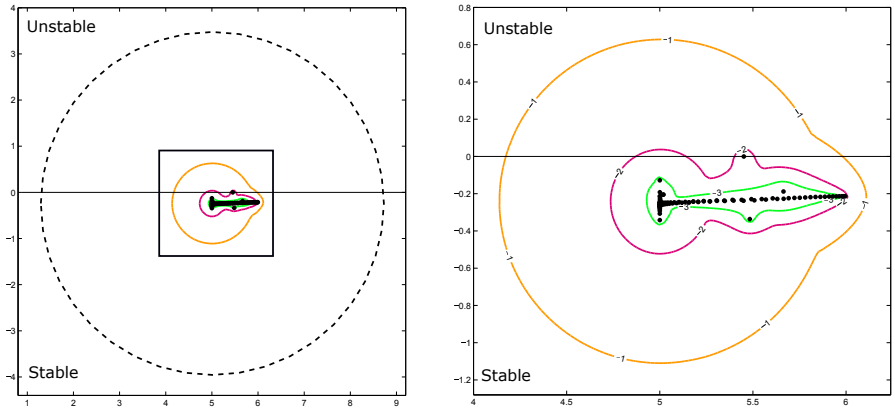

(b)

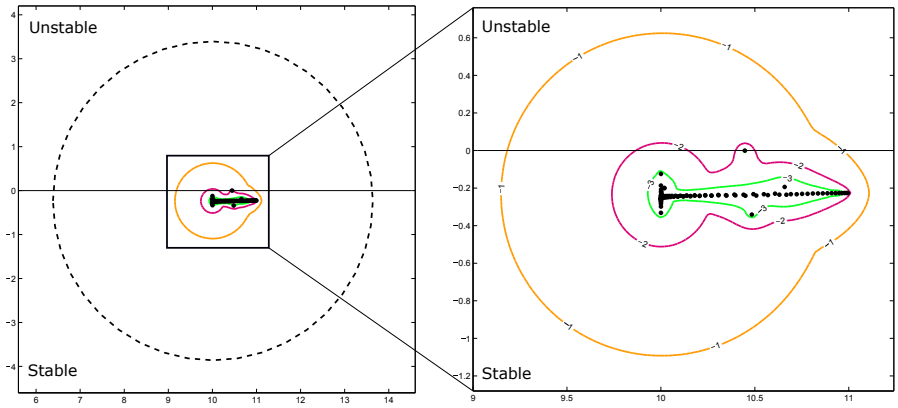

(c)

Figure 4.8: Spectral portraits of asymptotically stable cases for the jet velocity profile with constant depth and (a) $U_1 = 1$, (b) $U_1 = 5$, (c) $U_1 = 10$

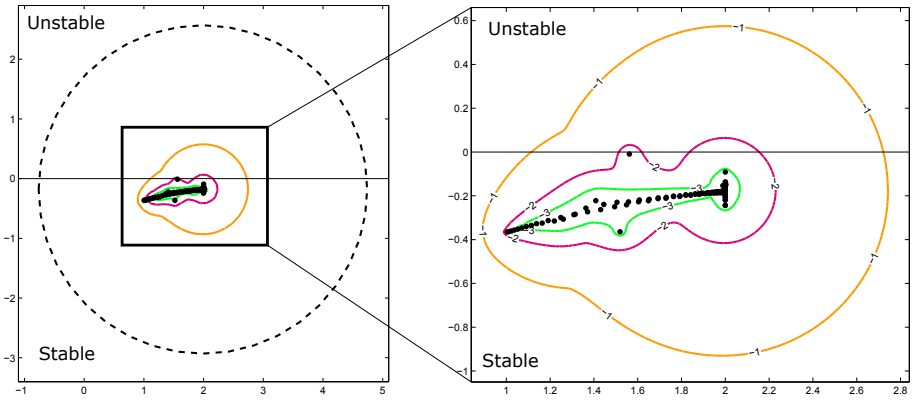

(a)

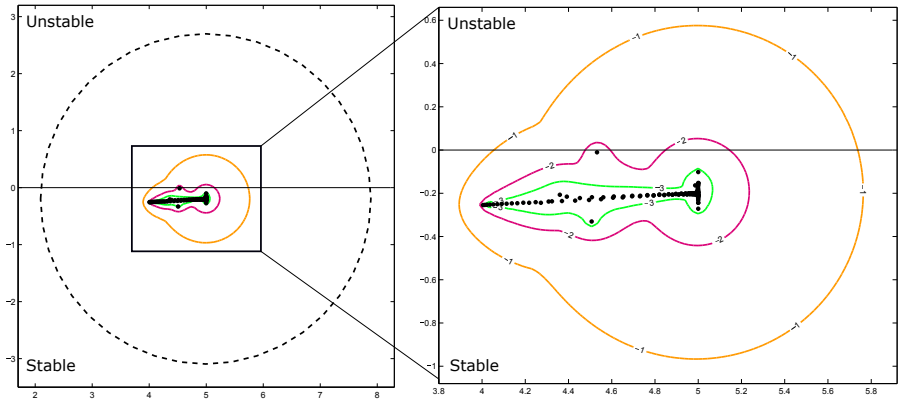

(b)

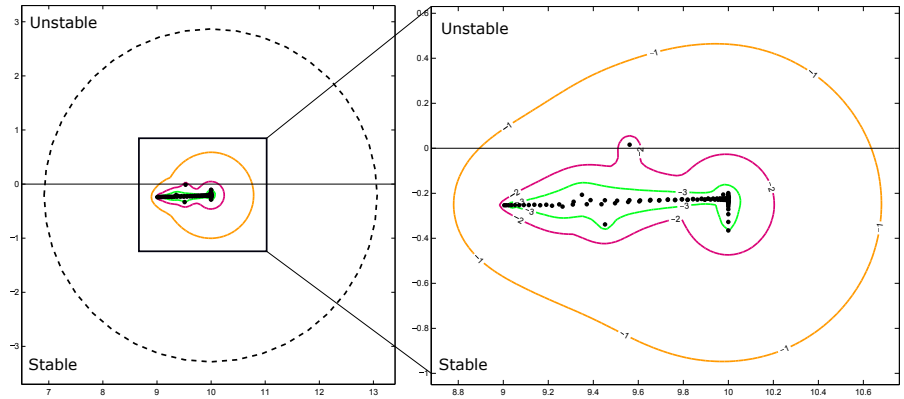

(c)

Figure 4.9: Spectral portraits of asymptotically stable cases for the wake profile with constant depth and (a) $U_a = 2$, (b) $U_a = 5$, (c) $U_a = 10$

4.5 Transient Energy Growth

From the spectral and pseudospectral portraits of the asymptotically stable cases, it can be concluded that the initial energy growth can be expected. The actual energy of the perturbations is proportional to and can be derived from the growth function, which is the norm of the matrix exponential of the linear operator as a function of time, as mentioned in Chapter 3. The growth function for the asymptotically stable cases, for which the spectra and pseudospectra are computed, are presented in this section.

Figure 4.1 shows the growth function calculated over time. As expected, there is initial energy growth which reaches a peak before the energy eventually dissipates. This case confirms that the linear modal stability only shows asymptotic stability while finite time energy behaviour is obtained through nonmodal analysis. Similar to the modal analysis results which show that the critical bed friction number for the cases of $U_a = 5, 10$ are almost identical, the growth functions are also identical, overlapping each other. The numerical abscissa values is higher for the case of $U_a = 1$ compared to $U_a = 5, 10$, which is reflected in the slope of initial energy growth. The growth function for $U_a = 1$ increases at a faster rate than $U_a = 5, 10$. However, the energy peaks for the cases of $U_a = 5, 10$ are higher. In terms of dissipation, the case of $U_a = 1$ takes longer to and approaches zero slower than $U_a = 5, 10$.

The transient evolution of energy for the jet profile is presented in figure 4.11. The initial growth and energy peak are observed as expected. The peak values, however, are slightly lower than that of the mixing layer profile. The decrease in the numerical abscissa values with increase in ambient velocity is also reflected in the slopes of the energy curves. The rate of energy growth for $U_a = 1$ is higher but the peak is lower compared to $U_a = 5, 10$. The cases for $U_a = 5, 10$ are almost the same with $U_a = 5$ having slightly higher values in the dissipation phase after $t = 15$. The dissipation rate of all the values seem to be more or less the same up to $t = 15$, after which it decreases dramatically for $U_a = 5, 10$ and there is a much smaller second peak for $U_a = 1$ a. The dissipation rate for $U_a = 1$ after $t = 20$ is comparable with the other cases. Figure 4.11 shows only up to $t = 60$ to highlight the behaviour at $t \to 0$, but the dissipation occurs over a longer period of time, with the energy

eventually approaching zero at around $t = 200$. This is much slower compared to the mixing layer case, for which the dissipation is captured within $t = 1 - 60$.

The wake velocity profile exhibited similar transient behaviour in the perturbation energy to the mixing layer and the jet profile as shown in figure 4.12. The numerical abscissa of the different ambient velocities are also seen in the variation of the slopes. The growth rate of energy for $U_a = 2$ is larger than $U_a = 5, 10$ but the peaks are more or less the same in all cases. The peaks for $U_a = 5, 10$ are more short lived and the energy dissipation started at an earlier time than $U_a = 2$, although the rate of dissipation is more or less equal. After $t = 20$ the dissipation rate of energy decreased but remained approximately the same. Similar to the jet profile, the energy dissipation of the wake profile also takes much longer than the mixing layer profile with the growth function approaching zero at around $t = 200$.

4.6 Summary

The traditional linear modal stability analysis of different shallow flows is conducted with different ambient velocity parameters. The fastest growing modes were evaluated for their growth rates as a function of bed friction. Linearly decreasing trends of the normalized growth rates are observed with increasing bed friction, which is in agreement with literature.

The critical cases, for which the growth rate approaches zero, are computed in terms of the critical bed friction number and the wavenumber of the fastest growing mode. The results of the modal stability analysis is generalized into stability regions, which showed parabolic regions of instability.

Nonnormality of the linear operator, which is a major reason for transient perturbation growth, is computed for the critical cases. The results show that the condition number for all the critical cases are greater than one, which suggests nonnormality.

The nonmodal stability metrics such as the pseudospectra, numerical abscissa were calculated for the critical cases. It is shown that the numerical abscissa, which is the rate of initial energy growth, extends into the unstable half-plane for all critical cases. The pseu-

dospectra of different order perturbation where also seen to be crossing over to the unstable half-plane, despite the spectrum entirely located in the stable half-plane.

By analyzing the transient energy growth, the stability behaviour of the system in finite time is observed. The perturbation energy grows in and reaches a peak before dissipating as $t \to \infty$. Although decrease in energy growth is observed in all cases, the magnitude and dissipation were very different.

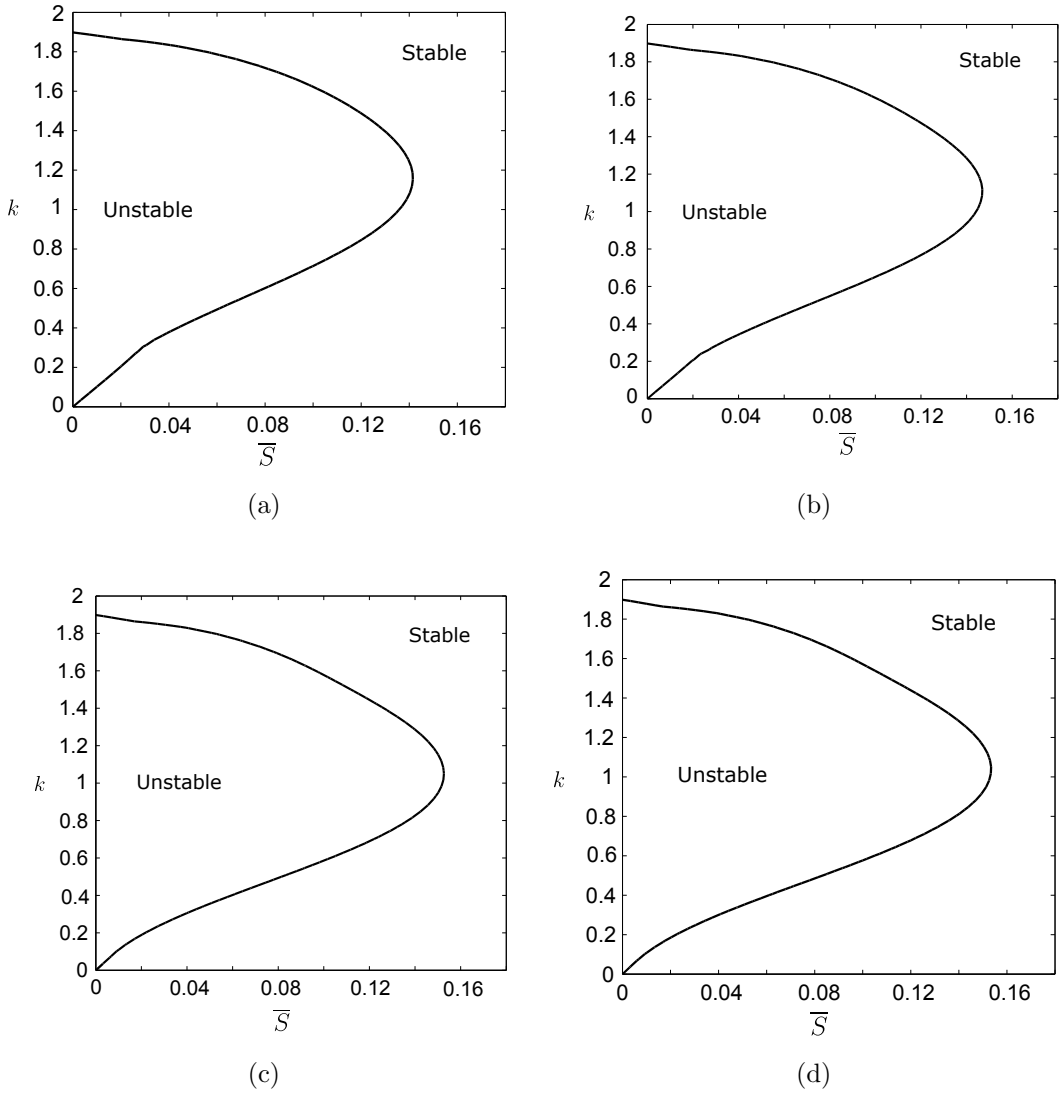

Figure 4.5: Unstable regions in the S-k space obtained from linear modal stability analysis for the jet profile with (a)$U_a = 0.5$, (b)$U_a = 1$, (c)$U_a = 5$, (d) $U_a = 10$

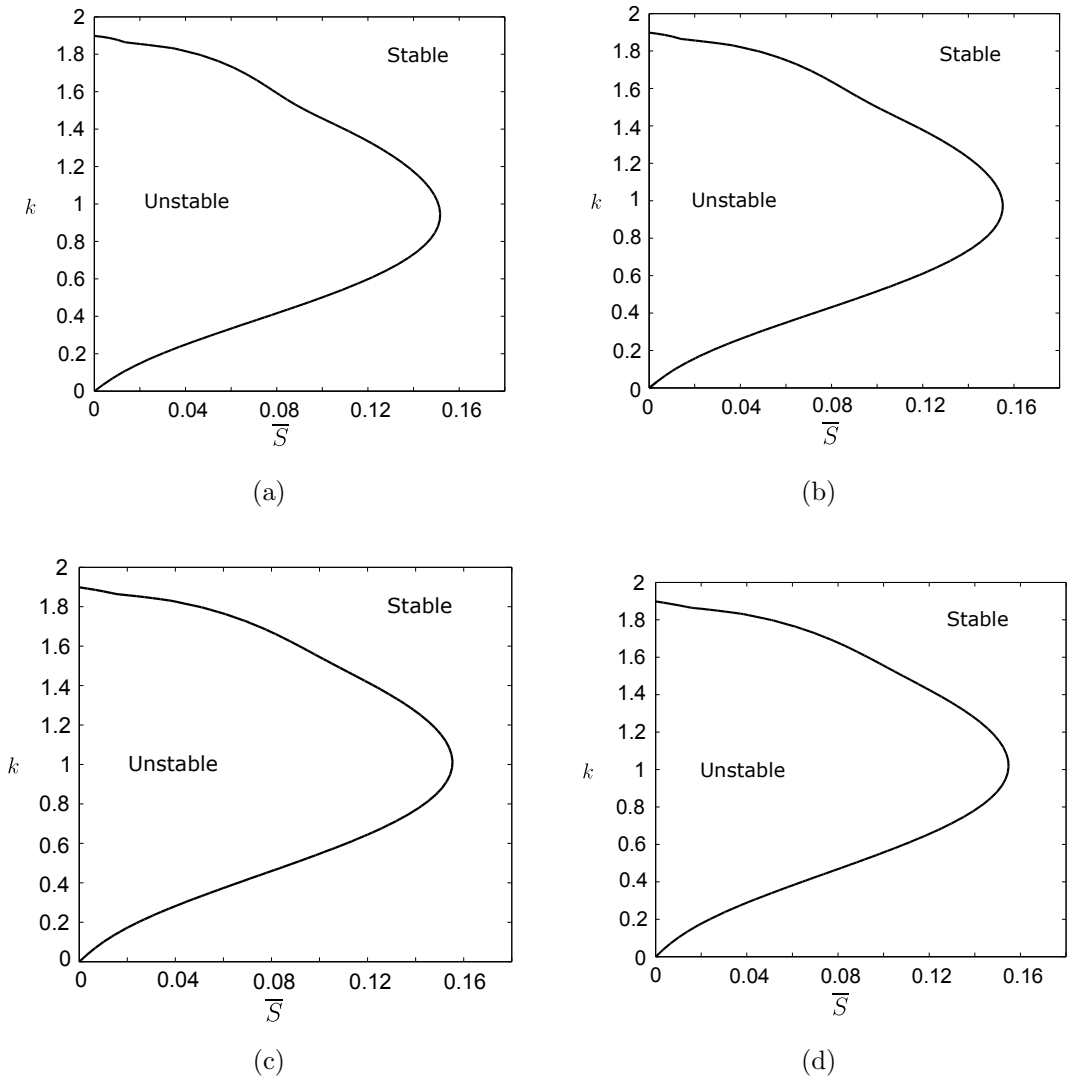

Figure 4.6: Unstable regions in the S-k space obtained from linear modal stability analysis for the wake profile with (a)$U_a = 1.5$, (b)$U_a = 2$, (c)$U_a = 5$, (d) $U_a = 10$

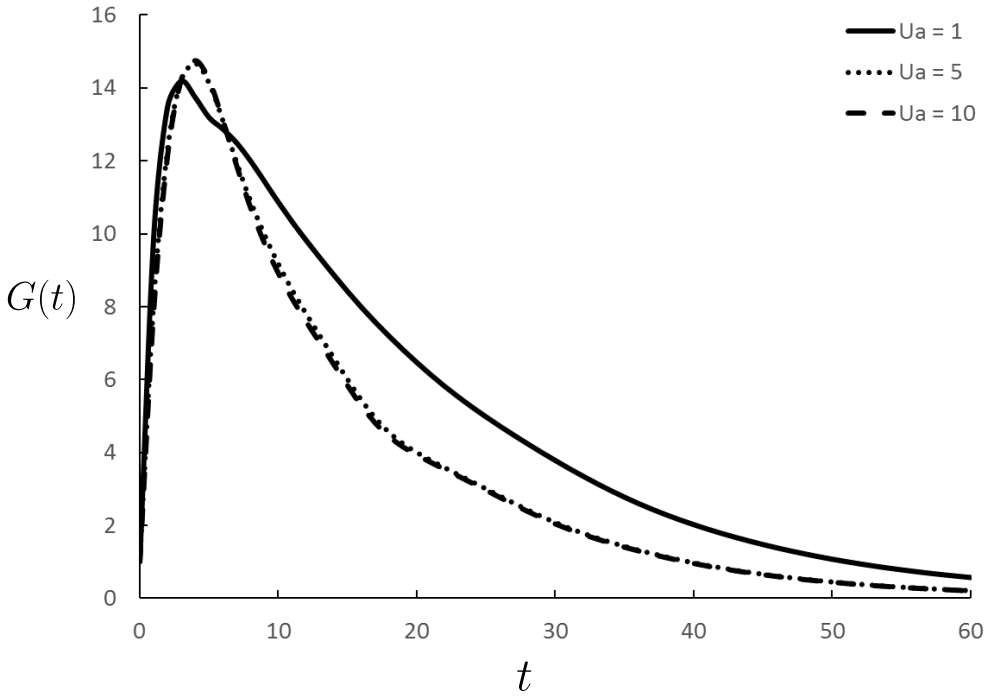

Figure 4.10: Transient energy amplification of asymptotically stable cases for the mixing layer profile with constant depth for $U_2 = 1, 5, 10$

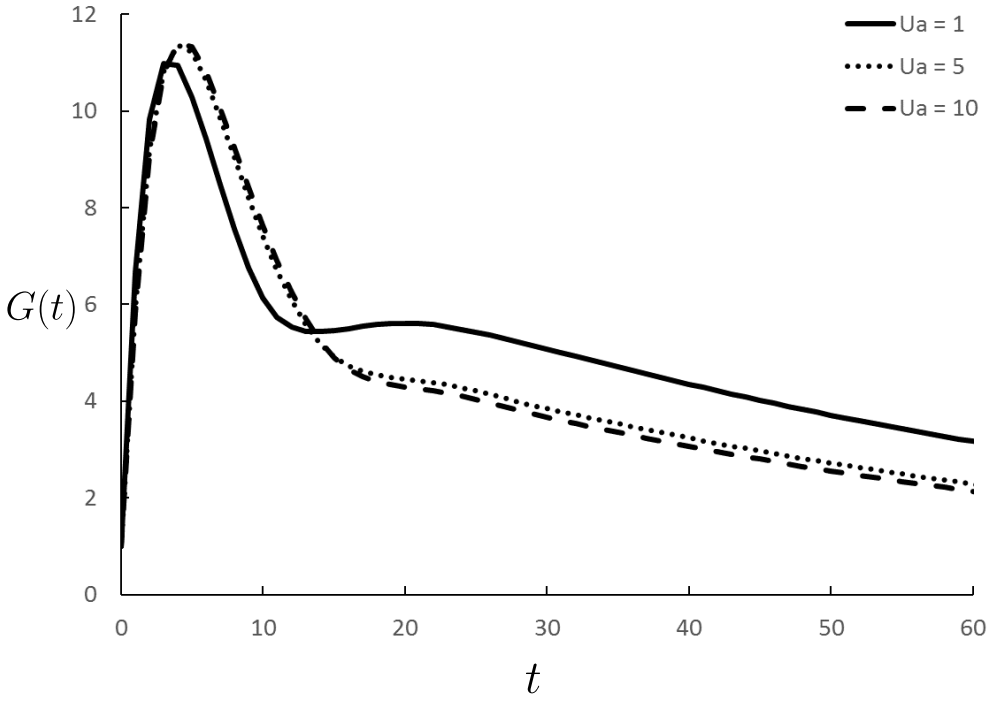

Figure 4.11: Transient energy amplification of asymptotically stable cases for the jet profile with for $U_1 = 1, 5, 10$

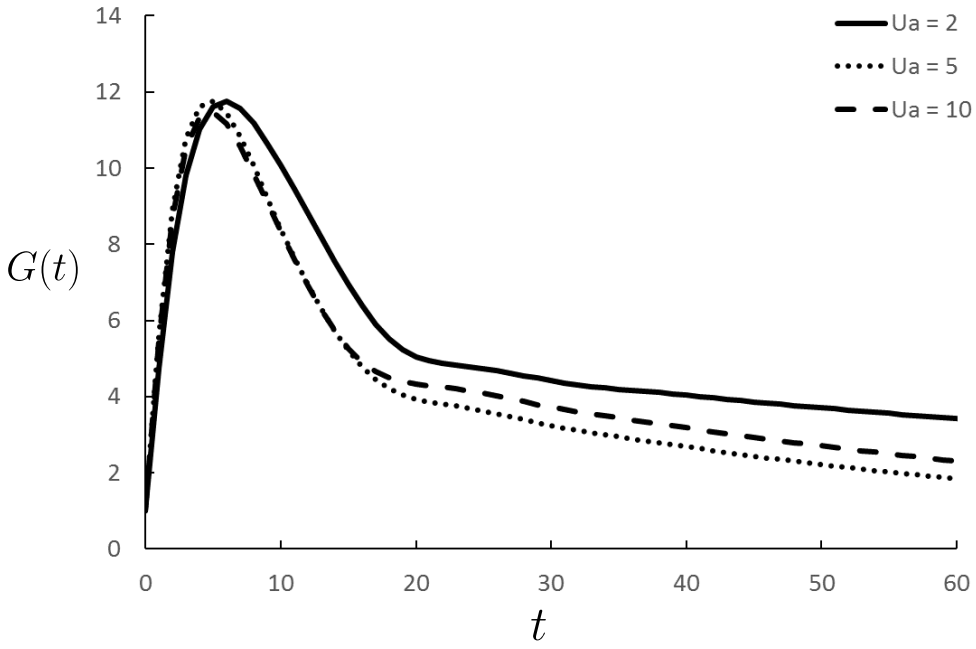

Figure 4.12: Transient energy amplification of asymptotically stable cases for the wake velociy profile for $U_1 = 2, 5, 10$

Chapter 5

Generalization of Nonmodal Stability

The nonnormality and transient perturbation energy growth of the critical cases have been shown in Chapter 4. In this chapter, the nonmodal stability analysis is expanded and generalized into the S-k space. The nonnormality, evaluated using the condition number, is presented, followed by the nonmodal stability regions, in which initial energy growth is expected.

5.1 Nonnormality of the Matrix Operator

The variation of the condition of number of $\mathbf{C}$ is evaluated in the S-k space for the mixing layer, jet and wake profiles with the higher three values of ambient velocities. For a matrix to be normal, the condition number is equal to unity.

Figure 5.1 shows the condition numbers evaluated for the mixing layer profile. For all ambient velocity parameters, the condition number is greater than one for all points in the S-k space in the considered range. Overall, the lower condition numbers are located at the upper left corner, corresponding to higher wavenumbers and lower bed friction. In contrast, the highest condition numbers are found at the bottom right corner, i.e. higher friction and lower wavenumbers. For $U_a = 1$ the minimum condition number is greater than two, while for the other two cases ($U_a = 3, 10$), the minimum was lower, between 1 and 1.3. The

contours are more distributed for the lower ambient velocity parameters and the become more concentrated to the bottom as the ambient velocity parameter increases.

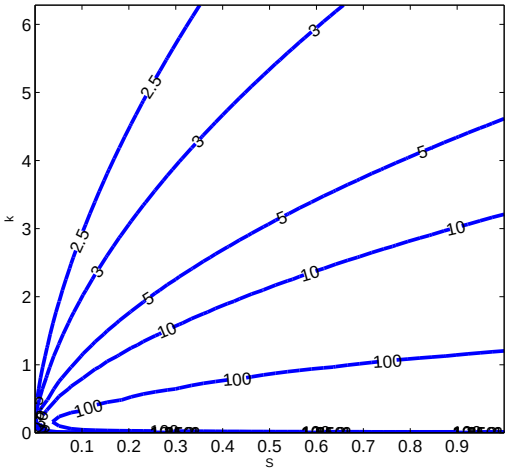

(a)

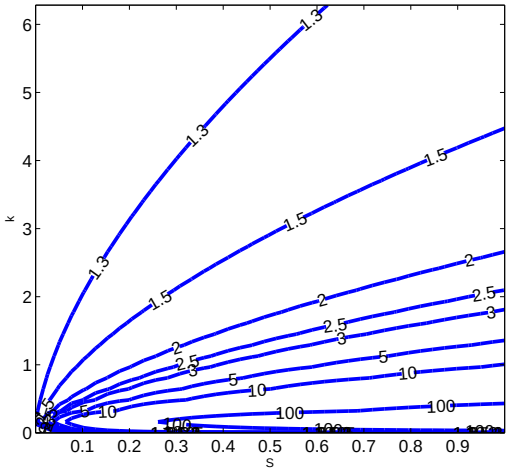

(b)

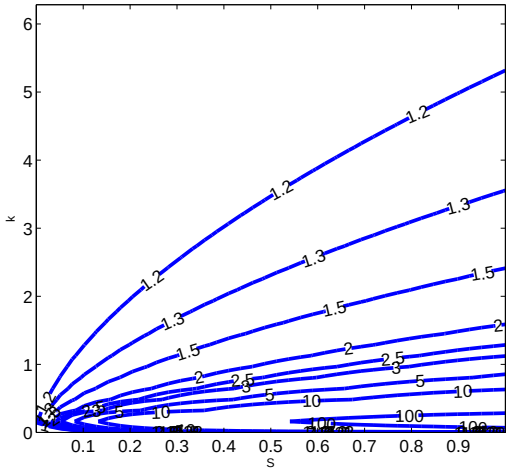

(c)

Figure 5.1: Condition numbers for the mixing layer profile with (a)$U_2 = 1$ (b) $U_2 = 5$(c) $U_2 = 10$

The condition numbers computed for the jet profile are shown in figure 5.2. The trends are very similar to that of the mixing layer profile. The minimum value of condition number in the S-k space decreases with increase in the ambient velocity parameter. The near-diagonal

isolines show that the upper left region has lower condition numbers while the lower right region has the highest condition numbers. The spread of the contour lines also behaves similarly to the mixing layer profile with the contours becoming more concentrated toward the lower right corner with the increase of the ambient velocity parameter.

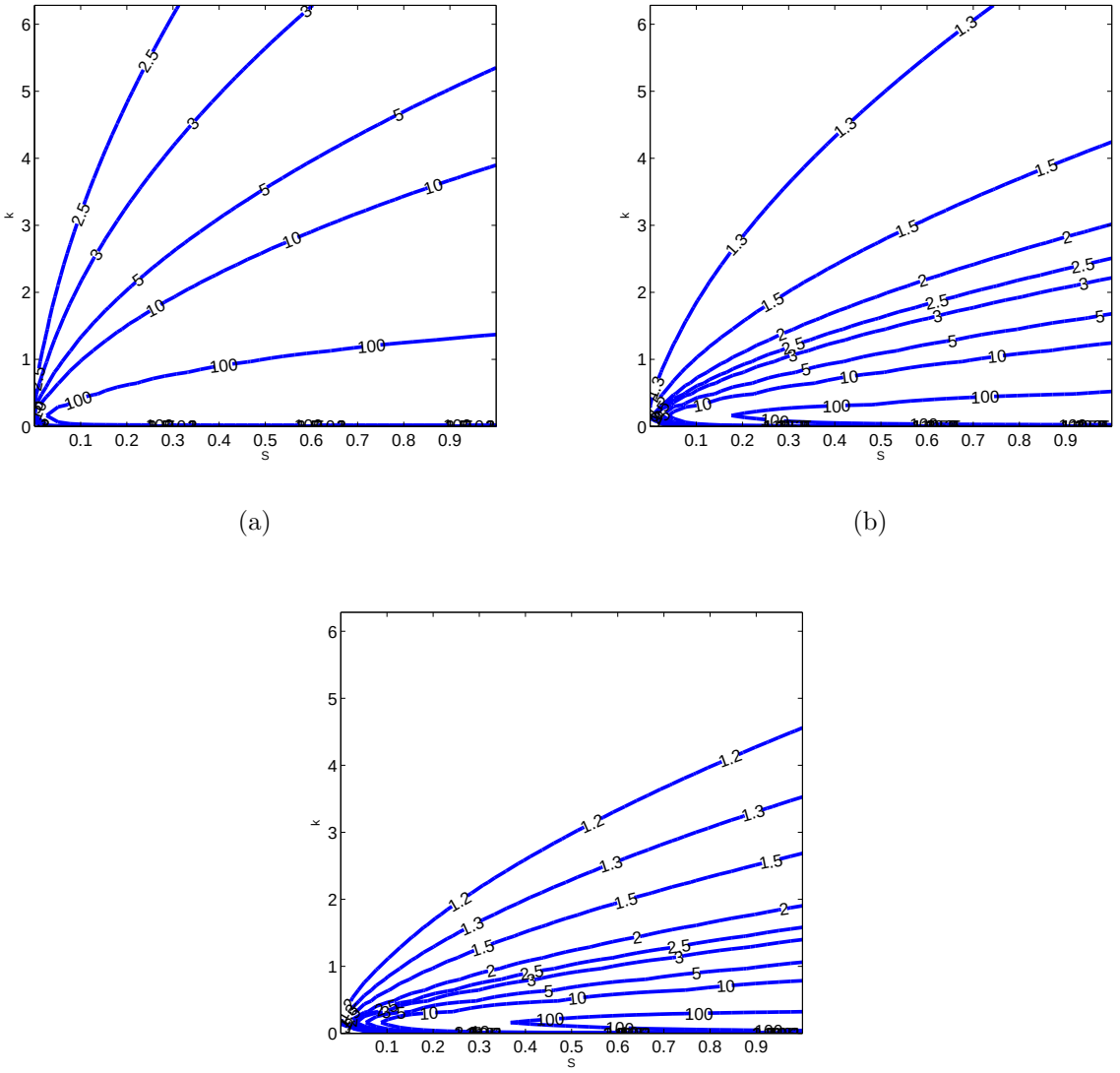

(a)

(b)

(c)

Figure 5.2: Condition numbers for the jet profile with(a)$U_2 = 1$ (b) $U_2 = 5$(c) $U_2 = 10$

Similarly, the condition numbers for the wake profile are present in figure 5.3. The plots are very similar to those of the mixing layer and jet profiles. The contours are seen in the

form of near-diagonal curves with lower values located at the top left corner and higher values at the bottom right corner. The minimum values also decreased from 2-2.5 for $U_a = 2$ to 1-1.3 for $U_a = 5$ and 1-1.2 for $U_a = 10$. The variation in the spread of the contours, however, is different with the most spacing observed at $U_a = 5$.

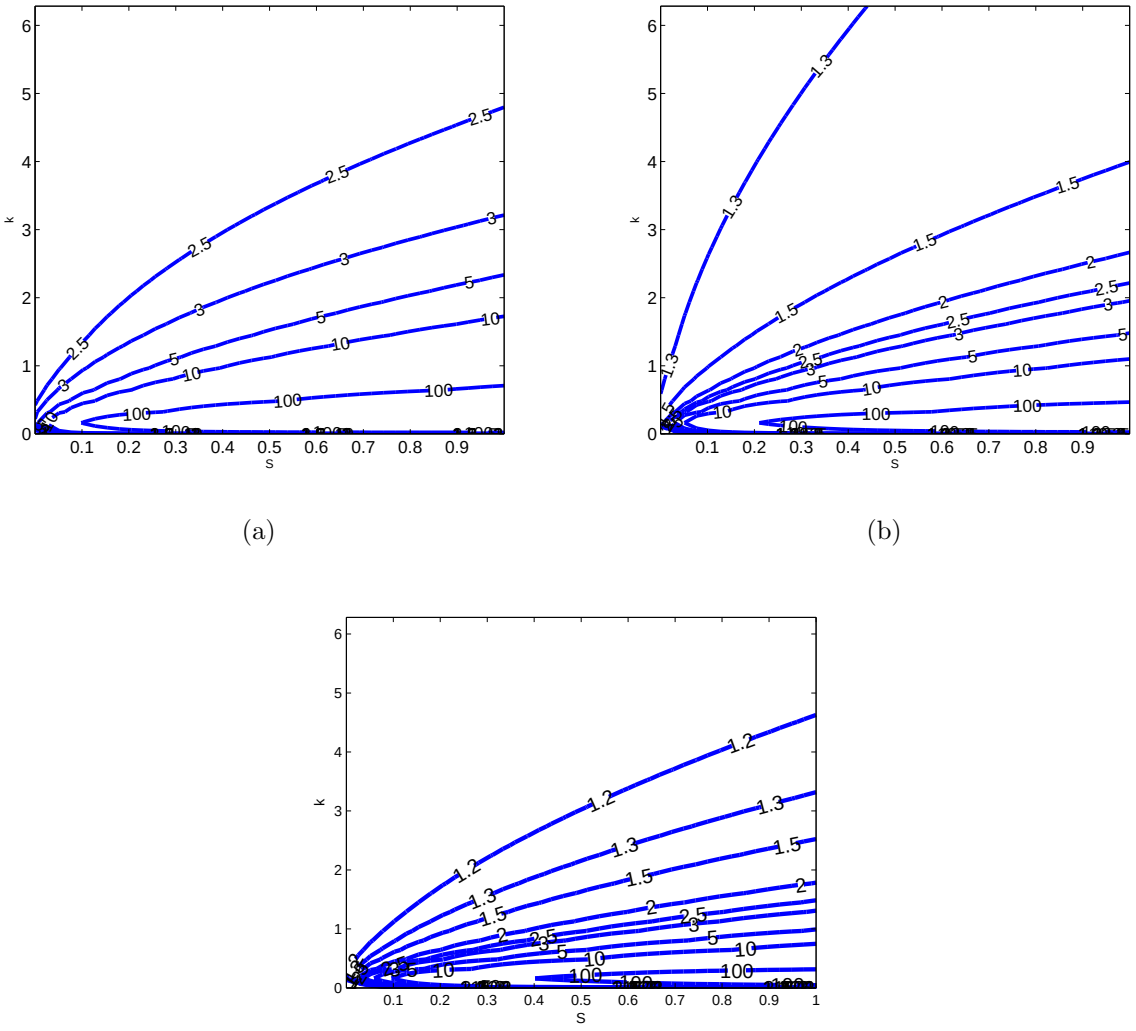

(a) (b)

(c)

Figure 5.3: Condition numbers for the wake profile with(a)$U_2 = 1$ (b) $U_2 = 5$(c) $U_2 = 10$

All three velocity profiles of shallow flows showed that the condition number is greater than one for the extent of S-k considered. The general trend of the contours in all cases followed near-diagonal curves increasing from top left to bottom right. It can be said that

high bed friction with low wavenumbers produces highest condition numbers and thus, the highest deviation from normality. Transient growth is therefore expected everywhere in the S-k space shown.

5.2 Asymptotic and Finite time Stability Regions

The stability, or rather the growth of perturbation energy, is generalized in the S-k space for the three velocity profiles in considerations. The domain shown for the stability regions in this section is $\{(S,k) \in \mathbb{R} \quad | \quad 0 < S < 1 \quad and \quad 0 < k < 2\pi\}$. The modal stability regions shown in Chapter 4 are superimposed on the nonmodal stability contours, showing the magnitude of the numerical abscissa. Within the modal stability region,in which the fastest growing mode dominates, the energy will grow exponentially as $t \to \infty$ and outside of this region the energy growth occurs at the rate equal to the numerical abscissa on the log scale.

The stability regions for the mixing layer profile are presented in figure 5.4. It is clearly shown that the behaviour of perturbation growth in finite time can be seen more clearly with nonmodal stability analysis. It is actually unstable everywhere in the extent of the S-k space shown with a high variation of numerical abscissa values, hence the log scale was used to plot the contours. The contours for numerical abscissa values greater than one resembles the contours of condition numbers show in the previous section. The highest initial growth is also seen to be present in the region of highest condition numbers. The lower values are also seen to concentrate around the top left corner, as seen by the 0.1 contour line. The ambient velocity increase does not seem to affect the initial energy growth, as evident by the almost identical contours for all three cases shown. It is also noteworthy that the contours are plotted over a significantly larger area than the modal stability region to showcase the range of S and k values beyond this unstable region that leads to initial energy growth.

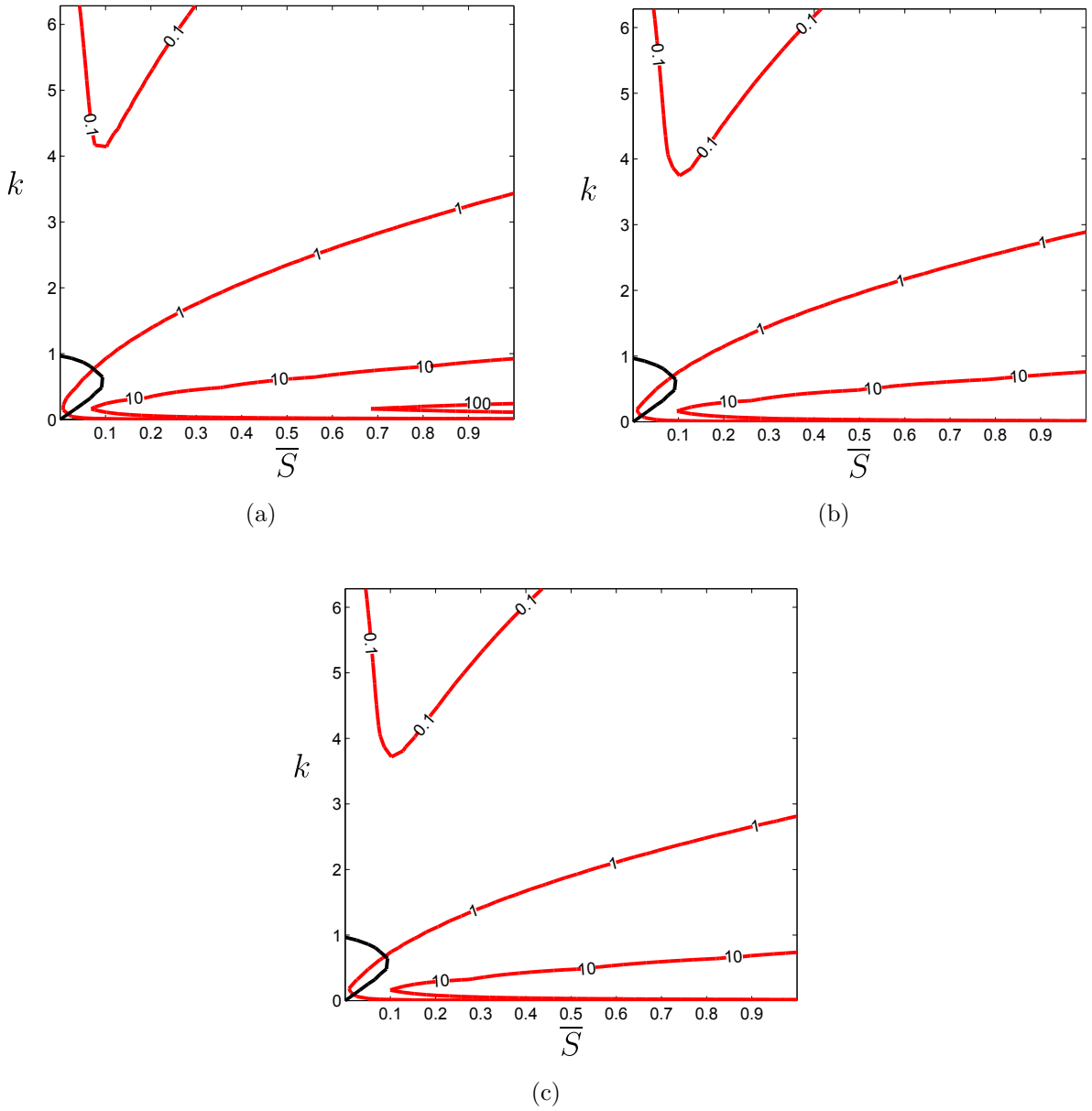

(a) (b)

(c)

Figure 5.4: Asymptotic and finite time stability regions for the mixing layer profile with (a)$U_2 = 1$ (b) $U_2 = 5$(c) $U_2 = 10$

The asymptotic and finite stability regions for the jet profile are given in figure 5.5. The general trend of the contour lines are reasonably similar to those of the mixing layer profile with numerical abscissa values greater than zero in all points in the plot. The highest transient growth, again, is in the lower right corner of the S-k space where the values of S are

high and k is low. Unlike the mixing layer profile, the contour for 0.1 is absent showing that the minimum value of the numerical abscissa is between 0.1 and 1. The contours remained almost unchanged with the increase of the ambient velocity parameter.

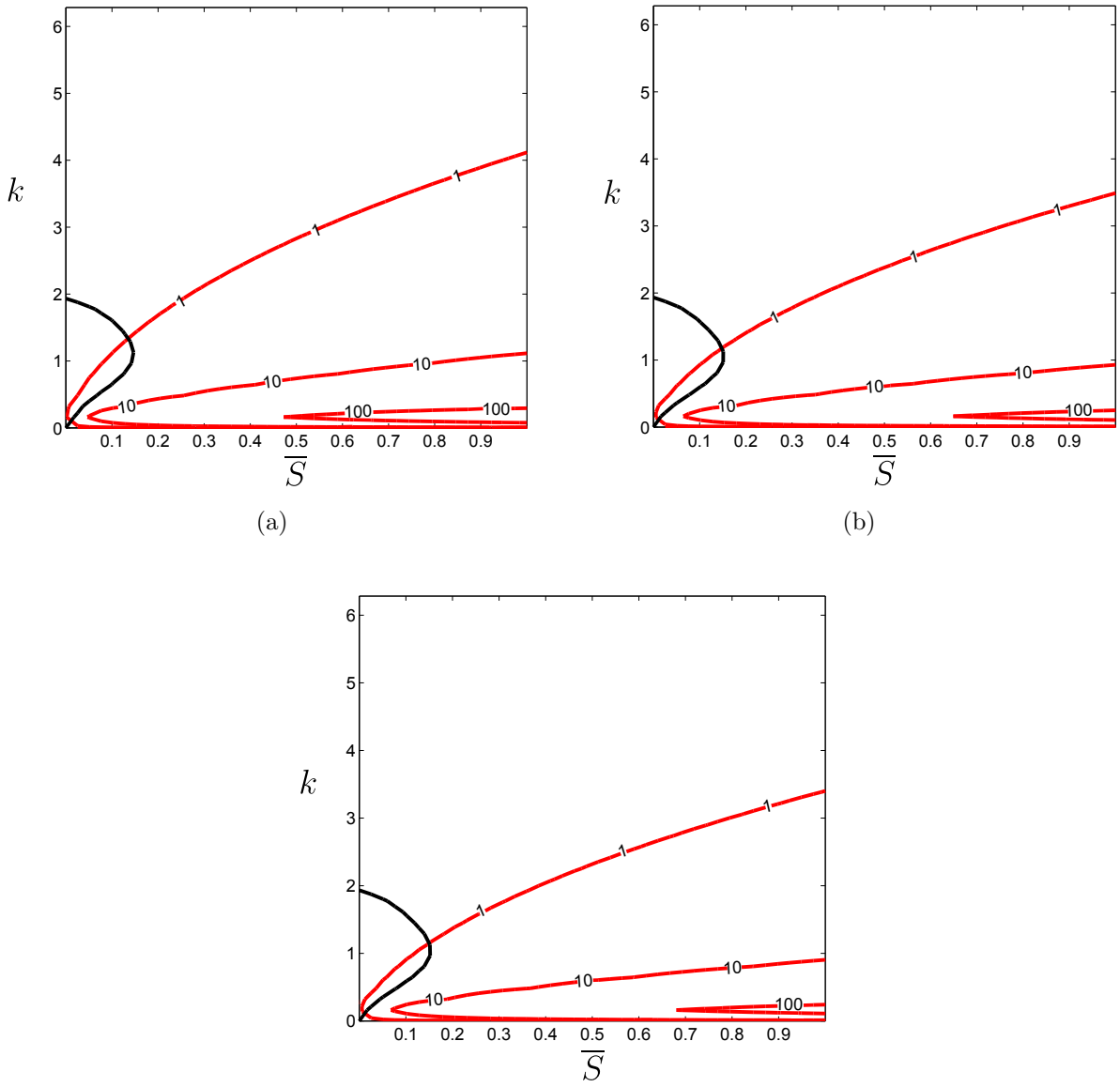

(a) (b)

(c)

Figure 5.5: Asymptotic and finite time stability regions for the jet profile with (a)$U_2 = 1$ (b) $U_2 = 5$(c) $U_2 = 10$

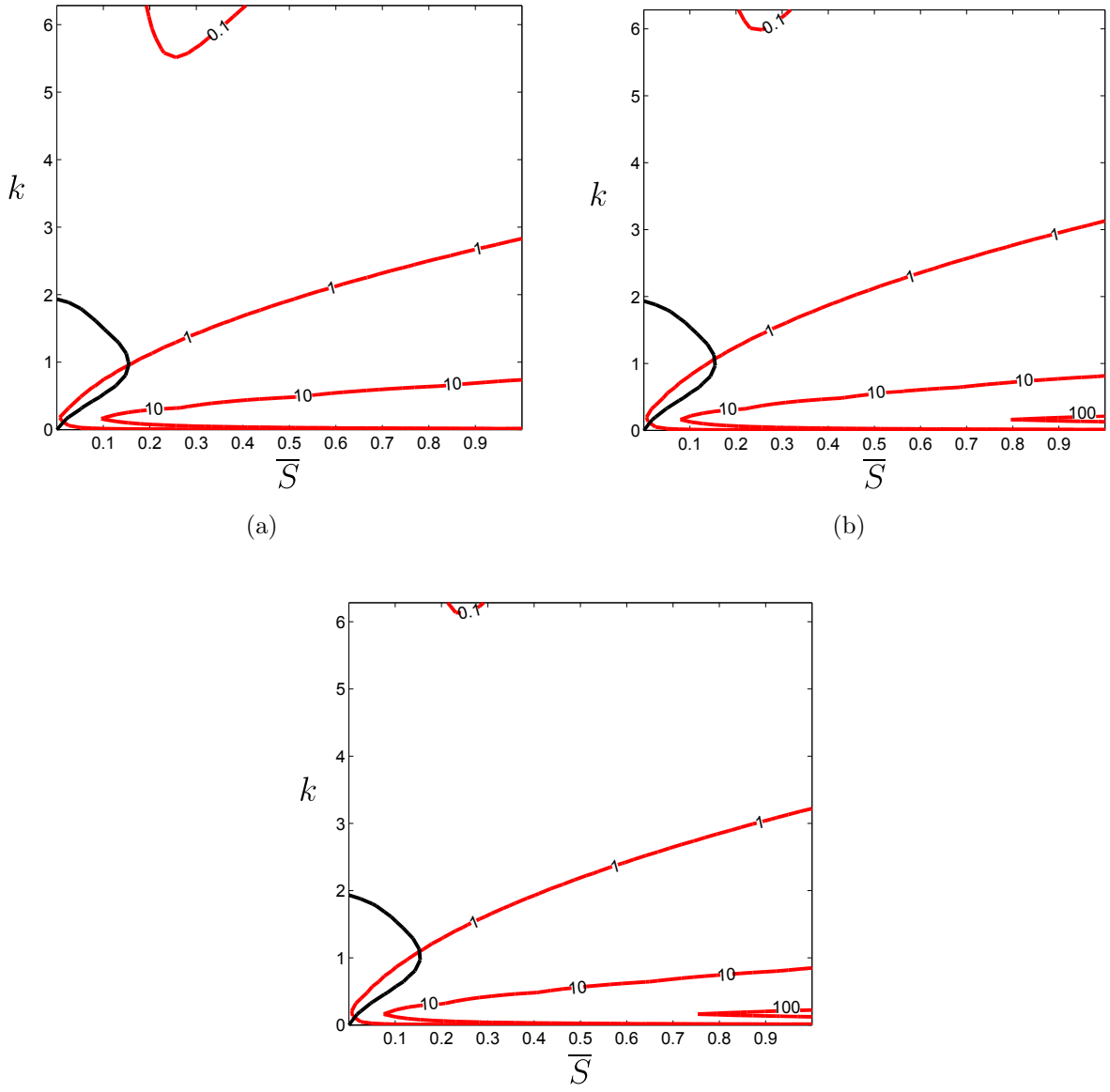

(a) (b)

(c)

Figure 5.6: Asymptotic and finite time stability regions for the wake profile with (a)$U_2 = 1$ (b) $U_2 = 5$(c) $U_2 = 10$

Figure 5.6 shows the stability plots for the the last case, the wake profile. The overall trend is very similar to the mixing layer and jet profile as shown above. The higher contours also reflect the condition numbers as shown in section 5.1, where the larger values are at the lower right corner. The lowest values, however, are on the upper side of the graph, shown by

the contour of 0.1, slightly off center. These regions are noticeably small compared to the other regions. The ambient velocity increase does not effect the contours significantly as in the cases of the mixing layer and jet profiles.

5.3 Summary

This chapter is dedicated to generalize the initial growth of perturbation energy in the S-k space. Section 5.1 expands the computation of the condition number, a measure of nonnormality, in the same space. The results showed that in the limits of the S-k space evaluated, the condition number is greater than unity in all coordinates. This means that for all values of S and k reasonably concerned, modal stability does not give a complete picture of the behaviour of perturbations. Transient growth can be expected in finite time.

Section 5.2 presents the asymptotic stability regions superimposed on the contours of the numerical abscissa values, which are indicative of initial perturbation energy growth. The region is purposely selected to be much larger than the modal stability region to make the initial energy growth in the S-k space more evident. It can be seen in all cases that the numerical abscissa contours closely reflected the condition number contours with the highest values obtained from lower wave numbers and higher bed friction numbers. Bed friction is generally thought of as stabilizing, meaning the growth of perturbations is suppressed with higher friction. However, it is shown that although asymptotic stability is achieved from higher bed friction, high transient growth may also be observed.

Chapter 6

Conclusion

6.1 Summary of Findings

The stability of shallow flows has been studied by many researchers for decades and the use of linear modal stability analysis is very prominently featured, alongside experimental and direct numerical simulations. However, there were many reports of discrepancies between experimental results and the predictions of linear stability analysis. A common example given is the transition Reynold's number difference between the observed flows and the stability analysis. The reason for this issue is attributed to the linearization process itself since many of the systems of equations used to describe fluid dynamics are nonlinear. Another explanation is based on the diagonalization process or the eigenvalue analysis.

In the eigenvalue analysis or modal analysis for evaluating the stability of dynamical systems, only the largest eigenvalue, representing the fastest growing mode or wave is considered. This eigenmode dominates the dynamics and its behaviour governs the stability behaviour. This may be true in some cases such as the Rayleight-Benard convection, but not for shear flows such as the Couette and Poiseulle flows. Trefethen et al. (1993), showed that this can be explained by the normality of matrix. Simply put, a normal matrix is one with orthogonal eigenvectors and nonnormality, meaning the eigenvectors are not orthogonal to one another, can lead to transient growth in finite time. Therefore, the results

of modal analysis portray the asymptotic faith of the perturbations and in finite time as $t \to 0$, the growth of perturbations may be observed. In the present study, shallow flows are represented by three different velocity profiles: the mixing layer profile, the jet profile and the wake profile and evaluated for their stability behaviour with both modal and nonmodal approaches.

A modal analysis was first conducted on the three shallow flow velocity profiles. The purpose of this analysis is to determine the critical cases from modal analysis. The ambient velocity parameters were varied and the results were parametrized with the bed friction number at inflection point $\overline{S}$. The growth rate of the fastest growing mode, calculated from the imaginary part of the temporal frequency, is normalized using the derivative of the velocity profile at the inflection point. For all velocity profiles, the normalized growth rates decreased linearly as a function of the bed friction number and the critical bed friction numbers increased in ambient velocity parameters. The increase in ambient velocity parameter makes the system mores unstable and so higher bed friction is required to stabilize the flow. This can also be seen in the plot of stability regions in which the parabolic unstable region is larger for higher ambient velocity profiles. These results are consistent with the findings of Chu et al. (1991) and Ghidaoui and Kolyshkin (1999).

The critical cases from the modal analysis, which correspond to a specific point in the S-k space, have a matrix operator $\mathbf{C}$. The nonmorality of $\mathbf{C}$, which is an indication that transient growth, is evaluated using the condition number as described in Trefethen and Embree (2005). If the condition number is greater than unity, the eigenvectors are nonorthogonal and thus transient growth may occur. Consequently, the modal analysis results only describe the asymptotic behaviour of the perturbations. For all the critical cases, it was seen that that the condition numbers were all greater than unity and the evaluation of these cases in the nonmodal approach is warranted. The metrics used in nonmodal analysis are the pseudospectra and the numerical abscissa. These are shown as spectral and pseudospectral portraits in the complex plane. For the critical cases, the spectrum is seen to be entirely enclosed in the stable half-plane with the fastest growing mode on or very close to the

stability margin. However, the pseudospectra corresponding to the perturbations of the order $10^{-1}, 10^{-2}$ and 0^{-3} are shown and protruding into the unstable half-plane. This means that the eigenvalues can deviate and shift into the unstable half-plane if perturbed. The pseudospectral can also be used to calculate the extend of perturbation energy growth for the corresponding order of perturbation. The numerical abscissa is also seen to be protruding into the unstable half-plane. The numerical abscissa is the slope of the initial energy growth on the log scale and so the larger the numerical abscissa, the faster the energy growth at $t \to 0$. For all the critical cases, the numerical abscissa is much larger than the pseudospectra of 10^{-2}.

The transient energy growth of the perturbations is calculated using the growth function, which is the maximum energy optimized for all initial conditions. The transient energy growth is shown for selected critical cases and the perturbation energy can be seen to increase in time and reaches a peak before decaying. The numerical abscissa is higher for lower ambient velocity parameters, which is reflected in the growth functions. The slope of the initial energy increase is steeper for lower ambient velocity values but interestingly the peak is not necessarily higher. The dissipation for the mixing layer profile, in general, happens faster than the jet and wake profiles.

The results are taken beyond the critical cases and generalized into the S-k space. As mentioned earlier, the condition number is an indication of nonnormality and by extension transient dynamics in finite time. Therefore, the condition number is evaluated in the S-k for the three shallow flow velocity profiles for different ambient velocities. The results show that in the S-k space considered, that is $\{(S,k) \in \mathbb{R} \quad | \quad 0 < S < 1 \quad and \quad 0 < k < 2\pi\}$, the condition number is always greater than unity at all points in the space. Some general trends include the near-diagonal isolines of conditions numbers with the highest condition numbers located at the bottom of the S-k space where wavenumbers are lower but bed friction is higher. The lower bound of the condition number decreased with ambient velocity parameter.

Finally, the numerical abscissa values are also calculated for the S-k space and superim-

posed on the unstable region obtained from modal analysis. These clearly show the region in which the fastest growing mode governs and the perturbation energy will grow exponentially and the outer regions in which the perturbations decay at $t \to \infty$ but transient dynamics occur at $t \to 0$. The contours of the numerical abscissa closely reflect that condition numbers and are generally near-diagonal with higher values at the lower right corner. The ambient velocity parameter has little effect on the contour lines which are very similar for all ambient velocity parameters. The numerical abscissa values are also positive in everywhere in the S-k space considered which means that initial energy growth everywhere to some extent. One major difference between the findings of modal and nonmodal analyses is that the stabilizing effect of bed friction is only in terms of the asymptotic time scale. In finite time, higher bed friction actually increases the initial rate of perturbation energy growth.

6.2 Novelty and Contribution

As mentioned in Chapter 2, linear stability analysis in the modal sense has been done in a variety of publications for shallow flows. A nonmodal approach has not been taken to evaluate the growth of perturbations in finite time to the best of the author's knowledge. The nonmodal approach and the behaviour of the perturbations in finite adds the traditional evaluation of the fastest growing mode and paints a bigger picture of the stability in shallow flows. Nonnormality of the matrix operators is the reason for the amplified energy at $t \to 0$ and it is shown to be the case for shallow flows in this study. This warrants for more nonmodal analysis. The pseudospectral portraits and the transient energy growth as well as the condition numbers and the nonmodal stability regions the presented in this study has also not been done for allow flows as far as the author knows.

6.3 Potential Expansion and Future Work

The current research can be expanded in many directions. One possible expansion is to consider the viscous stability problem with the Orr-Sommerfeld equation instead of the inviscid Rayleigh equation. It has been shown that the stability of shallow flows does not depend on the Reynold's number when it is over 1000, but that might just be the case for asymptotic stability. Transient dynamics has not been studied, let alone the viscous stability problem. Another possible addition to the work is the consideration of free surface. The rigid lid assumption has been thoroughly studied by Ghidaoui and Kolyshkin (1999) and it is shown that it is very good for weak shear flows for which the Froude number is small but the error can be very high otherwise. Therefore, the nonmodal approach with additional parameters such as Reynold's number and Froude number can give a more complete picture. The current research is focused on the temporal evolution of perturbations. Spatial growth can also be studied. The spatial stability problem is a nonlinear higher order eigenvalue problem and a nonmodal approach may be mathematically challenging but it is a possible area of expansion.

As for the nonmodal stability analysis itself, the current study only evaluates the response of the system to initial conditions. The perturbations only happen at $t = 0$. The response of the system to forcing at different times or periodically is also an interesting topic of research.

Other works that can be done are the experimental studies and direct numerical simulations to solidify the findings in this study. With the development of experimental technology such as PIV and LIF systems, the development of unstable flows is more easily visualized and can be a valuable addition to the current work. Direct numerical simulations can also be used to show the flow features.

On a final note, this study is done to demonstrate that shallow flows do exhibit transient temporal dynamics and that the linear modal stability can be complimented by the nonmodal stability analysis to give a more complete picture of the growth of perturbations. The author hopes that the current work will be expanded to better the understanding of shallow flow instabilities.

Bibliography

Batchelor, G. K. (1969). Computation of the Energy Spectrum in Homogeneous Two-Dimensional Turbulence, *Physics of Fluids* **12**(12): II–233.

Betchov, R. and Criminale Jr, W. (1966). Spatial instability of the inviscid jet and wake, *The physics of fluids* **9**(2): 359–362.

Browand, F. and Troutt, T. (1980). A note on spanwise structure in the two-dimensional mixing layer, *Journal of Fluid Mechanics* **97**(04): 771–781.

Carmer, C., Weitbrecht, V. and Jirka, G. (2001). On the genesis and fate of large coherent vortical structures in turbulent shallow wake flows, *Proc. 3rd International Symposium on Environmental Hydraulics, Tempe, USA*.

Chen, D. and Jirka, G. H. (1995). Experimental study of plane turbulent wakes in a shallow water layer, *Fluid Dynamics Research* **16**(1): 11–41.

Chen, D. and Jirka, G. H. (1997). Absolute and convective instabilities of plane turbulent wakes in a shallow water layer, *Journal of Fluid Mechanics* **338**: 157–172.

Chen, D. and Jirka, G. H. (1998). Linear stability analysis of turbulent mixing layers and jets in shallow water layers, *Journal of Hydraulic Research* **1686**(July).

Chen, D. and Jirka, G. H. (1999). LIF Study of Plane Jet Bounded in Shallow Water Layer, *Journal of Hydraulic Engineering* **125**(August): 817–826.

Chu, V. H. and Babarutsi, S. (1988). Confinement and Bed-Friction Effect in Shallow Turbulent Mixing Layers, *Journal of Hydraulic Engineering* **114**(10): 1257–1274.

Chu, V., Wu, J. and Khayat, R. (1983). Stability of turbulent shear flows in shallow channel, *Proc. XX Congress IAHR, Moscow, USSR*, Vol. 3, pp. 128–133.

Chu, V., Wu, J. and Khayat, R. (1991). Stability of Transverse Shear Flows in Shallow Open Channels, *Journal of Hydraulic Engineering* **117**(10): 1370–1388.

Dewals, B. J., Kantoush, S. A., Erpicum, S., Pirotton, M. and Schleiss, A. J. (2008). Experimental and numerical analysis of flow instabilities in rectangular shallow basins, *Environmental Fluid Mechanics* **8**(1): 31–54.

Dracos, T., Giger, M. and Jirka, G. H. (1992). Plane turbulent jets in a bounded fluid layer, *Journal of Fluid Mechanics* **241**(1992): 587–614.

Drazin, P. G. and Reid, W. H. (2004). *Hydrodynamic stability*, Cambridge university press.

Ghidaoui, M. and Kolyshkin, A. (1999). Linear Stability Analysis of Lateral Motions in Compound Open Chennels, *Journal of Hydraulic Engineering* **125**(August): 871–880.

Ghidaoui, M. S., Kolyshkin, A. A., Liang, J. H., Chan, F. C., Li, Q. and Xu, K. (2006). Linear and nonlinear analysis of shallow wakes, *Journal of Fluid Mechanics* **548**: 309–340.

Ghidaoui, M. S., Lam, M. Y. and Liang, J. H. (2012). Onset and development of instabilities in shallow shear flows, *Environmental Fluid Mechanics, Memorial Volume in Honour of Professor Gerhard H. Jirka, edited by W. Rodi and M. Uhlmann (CRC Press, 2012)* pp. 51–71.

Ghidaoui, M. S. and Liang, J. H. (2008). Investigation of shallow mixing layers by BGK finite volume model, *International Journal of Computational Fluid Dynamics* **22**(7): 523–537.

Grosch, C. E. and Salwen, H. (1975). An experimental investigation of the stability of plane Poiseuille flow, *Journal of Fluid Mechanics* **34**(1968): 731–751.

Herron, I. H. (1991). Observations on the role of vorticity in the stability theory of wall bounded flows, *Studies in applied mathematics* **85**(3): 269–286.

Huerre, P. and Monkewitz, P. A. (1990). Local and Global Instabilities in Spatially Developing Flows, *Annu. Rev. Fluid Mech.* **26**: 473–537.

Hussain, A. K. M. F. (1983). Coherent structures—reality and myth, *Physics of Fluids* **26**(10): 2816.

Jirka, G. H. (2001). Large scale flow structures and mixing processes in shallow flows, *Journal of Hydraulic Research* **39**(6): 567–573.

Khalil, H. K. (2002). Nonlinear systems.

Lin, C. (1955). *The Theory of Hydrodynamic Stability*, Cambridge monographs on mechanics and applied mathematics, University Press.

Lundbladh, A. and Johansson, A. V. (1991). Direct simulation of turbulent spots in plane Couette flow, *J. Fluid Mech* **229**(1991): 499.

Nachtsheim, P. R. (1964). *An initial value method for the numerical treatment of the Orr-Sommerfeld equation for the case of plane Poiseuille flow*, National Aeronautics and Space Administration.

Orr, W. M. (1907). The stability or instability of the steady motions of a perfect liquid and of a viscous liquid. part i: A perfect liquid, *Proceedings of the Royal Irish Academy. Section A: Mathematical and Physical Sciences*, JSTOR, pp. 9–68.

Orszag, S. a. (1971). Accurate solution of the Orr-Sommerfeld stability equation, *Journal of Fluid Mechanics* **50**(04): 689–703.

Patel, V. C. and Head, M. (1969). Some observations on skin friction and velocity profiles in fully developed pipe and channel flows, *Journal of Fluid Mechanics* **38**(01): 181.

Reddy, S. C. and Henningson, D. S. (1993). Energy growth in viscous channel flows, *Journal of Fluid Mechanics* **252**(April 2006): 209.

Reynolds, O. (1883). An experimental investigation of the circumstances which determine whether the motion of water shall be direct or sinuous, and of the law of resistance in parallel channels., *Proceedings of the royal society of London* **35**(224-226): 84–99.

Schmid, P. J. (2007). Nonmodal Stability Theory, *Annual Review of Fluid Mechanics* **39**(1): 129–162.

Shen, S. (2012). Calculated amplified oscillations in the plane poiseuille and blasius flows, *Journal of the aeronautical sciences* .

Socolofsky, S. a. and Jirka, G. H. (2004). Large-scale flow structures and stability in shallow flows, *Journal of Environmental Engineering* **462**(2004): 451–462.

Socolofsky, S. A., von Carmer, C. and Jirka, G. H. (2004). Shallow turbulent wakes: linear stability analysis compared to experimental data, *Shallow Flows: Research Presented at the International Symposium on Shallow Flows, Delft, Netherlands, 2003*, Taylor & Francis, p. 31.

Sommerfeld, A. (1908). Ein beitrag zur hydrodynamischen erklaerung der turbulenten fluessigkeitsbewegungen, *Atti del* **4**: 116–124.

Thomas, L. H. (1953). The stability of plane poiseuille flow, *Physical Review* **91**(4): 780–783.

Tillmark, N. and Alfredsson, P. H. (1992). Experiments on transition in plane Couette flow, *Journal of Fluid Mechanics* **235**(-1): 89.

Trefethen, L. N. (2000). *Spectral methods in MATLAB*, SIAM.

Trefethen, L. N. and Embree, M. (2005). *Spectra and pseudospectra: the behavior of nonnormal matrices and operators*, Princeton University Press.

Trefethen, L., Trefethen, A., Reddy, S. and Driscoll, T. (1993). Hydrodynamic stability without eigenvalues., *Science (New York, N.Y.)* **261**(5121): 578–584.

Uijttewaal, W. and Jirka, G. H. (2004). Shallow flows: a definition, *Shallow flows*, Taylor & Francis, chapter Introducti, pp. 1–13.

Uijttewaal, W. S. J. and Booij, R. (2000). Effects of shallowness on the development of free-surface mixing layers, *Physics of Fluids* **12**(2): 392.

van Prooijen, B. C. and Uijttewaal, W. S. J. (2002). A linear approach for the evolution of coherent structures in shallow mixing layers, *Physics of Fluids* **14**(12): 4105–4114.

Wolanski, E., Imberger, J. and Heron, M. (1984). Island wakes in shallow coastal waters, *Journal of geophysical research* **89**(C6): 10553–10569.

Wright, T. G. (2000). EigTool, http://www.comlab.ox.ac.uk/pseudospectra/eigtool/.